FABRICATION OF THREE-DIMENSIONAL NANOSTRUCTURES FOR THERMAL STUDY

BY

HA SEONG KIM

THESIS

Submitted in partial fulfillment of the requirements
for the degree of Master of Science in Materials Science and Engineering
in the Graduate College of the
University of Illinois at Urbana-Champaign, 2013

Urbana, Illinois

Adviser:

Professor Paul V. Braun

1. REPORT DATE **2013**	2. REPORT TYPE	3. DATES COVERED **00-00-2013 to 00-00-2013**

4. TITLE AND SUBTITLE **Fabrication of Three-Dimensional Nanostructures for Thermal Study**	5a. CONTRACT NUMBER
	5b. GRANT NUMBER
	5c. PROGRAM ELEMENT NUMBER

6. AUTHOR(S)	5d. PROJECT NUMBER
	5e. TASK NUMBER
	5f. WORK UNIT NUMBER

7. PERFORMING ORGANIZATION NAME(S) AND ADDRESS(ES) **University of Illinois at Urbana-Champaign,Department of Materials Science and Engineering,Urbana,IL,61801**	8. PERFORMING ORGANIZATION REPORT NUMBER

9. SPONSORING/MONITORING AGENCY NAME(S) AND ADDRESS(ES)	10. SPONSOR/MONITOR'S ACRONYM(S)
	11. SPONSOR/MONITOR'S REPORT NUMBER(S)

12. DISTRIBUTION/AVAILABILITY STATEMENT **Approved for public release; distribution unlimited**

13. SUPPLEMENTARY NOTES

14. ABSTRACT

15. SUBJECT TERMS

16. SECURITY CLASSIFICATION OF:			17. LIMITATION OF ABSTRACT	18. NUMBER OF PAGES	19a. NAME OF RESPONSIBLE PERSON
a. REPORT **unclassified**	b. ABSTRACT **unclassified**	c. THIS PAGE **unclassified**	**Same as Report (SAR)**	**50**	

ABSTRACT

Advance in nanotechnology has made a good understanding of high frequency phonon dominant, nanometer scale thermal transport a necessity. To study nanometer-scale thermal transport in three dimensions, three-dimensional nanostructured materials are needed. In this work, fabrication of sub 100 nanometer periodic dielectric three-dimensional structures and epitaxial nanostructures are discussed.

Using self-assembly of colloidal silica particles as a template, various dielectrics of interest were filled to create nanostructured dielectric materials. First, sub-100 nanometer silica nanoparticles were synthesized and used to assemble a colloidal crystal template, opals. Static silicon chemical vapor deposition filled the above templates with amorphous silicon and thermal annealing converted the amorphous silicon to polycrystalline silicon with an average grain size of 10 nanometers. Subsequent etching with dilute ethanolic hydrofluoric acid yielded periodic three-dimensional polycrystalline silicon nanostructures with characteristic skeleton size of around 20 nanometers. Using a similar colloidal crystal template made of 400 nanometer sized silica nanoparticles, cuprous oxide film was epitaxially grown into the template using electrodeposition.

These three-dimensional, sub-100 nanometer silicon nanostructures and three-dimensional epitaxial cuprous oxide nanostructures are similar to the length scale of the mean free path of the phonons. The nanostructures fabricated in this thesis provide fabrication tools to prepare samples which can be used to investigate the nanoscale phonon transport.

ACKNOWLEDGMENTS

I would first like to thank my advisor, Professor Paul Braun, for his support and for being a wonderful mentor. His advice, encouragement, and positive criticism helped me greatly during my time in his group and helped me mature not only as a scientific inquirer, but also as a person. My admiration and respect for him will long live with me throughout my life.

Next, I would like to thank my family for all the emotional support they provided me during the occasional rough times during my study at Illinois. Without their support, I would have faltered well short of what I am today.

Third, I would like to thank all my fellow Braun group members for being great labmates and colleagues. I especially want to thank Dr. Jinwoo Kim for his insightful research discussion and emotional support. I would like to thank Dr. Jiung Cho, Junjie Wang, Bibek Parajuli, and Hailong Ning for their experimental assistance and insightful discussions.

Lastly, I would like to thank the U.S. Air Force Office of Scientific Research which financially supported this work.

TABLE OF CONTENTS

CHAPTER 1

INTRODUCTION

1.1. Nanoscale Materials and Thermal Conductivity

Thermal management is crucial in numerous fields of engineering systems. For example, in micro- and nano-scale electronic devices, the efficient dissipation of heat is important since large concentrations of heat affect device properties and operation. With recent advances in the processing of dielectric materials such as silicon and devices in the nanometer scale, there is a growing need for a better understanding of thermal transport at the nanoscale [1].

Phonons, the quanta of lattice energy vibration, are the main energy carriers of heat within dielectric materials, whereas in metals, electrons carry most of the heat. Across the phonon spectra, the phonons which are responsible for carrying most of the heat through the lattice are high frequency phonons, typically on the order of THz [2, 3]. At room temperature, the mean free path of phonons responsible for thermal transport is around tens of nanometers for defect-free bulk crystals, and polycrystalline materials with defects can have phonon mean free paths much less than 10 nm.

As scientists access regimes where the materials are smaller than or comparable to the mean free path of the phonons using new fabrication tools, thermal properties unseen in the bulk materials have been reported. For example, until recently, the minimum thermal conductivity (Λ), which is defined traditionally by Fourier's Law of Heat Conduction as the rate of heat flow through a material in a temperature gradient, was believed to be set by the "amorphous limit" which describes the heat transport as a random walk of vibrational energy between the neighboring atoms [4]. Contrary to the knowledge, recent research showed that the nanoscale superlattice materials (Figure 1.1A) can have a lower thermal conductivity than the traditionally

believed "amorphous limit" (Figure 1.1B) [5, 6].   In other research works, scientists have utilized nanostructures to increase the phonon-boundary scattering mechanism (Figure 1.2) and reduce the thermal conductivity of materials and applied the structures towards high figure-of-merit thermoelectric materials [7 – 11].   As nanostructured materials reach the length scale of phonon mean free paths, traditional thermal transport approaches such as the Fourier's Law of heat conduction breakdown while giving rise to interesting thermal transport properties [2].

1.2 Phonon Coherence and Periodic Nanostructures for Phononic Crystal

Phonons, which have wide range of frequency from sound waves (Hz) to high frequency thermal phonons (THz), can interact coherently when the coherence length scales are larger than the size of the structure. Such coherent phonon interaction in a periodic manner can lead to a modified phonon dispersion relation and can open up a phononic band gap, similar to that of photons in semiconductors, in the material. Such phenomenon has been predicted theoretically for low frequency phonons, acoustic sound waves, in periodic structures and have been experimentally verified [12,13].

For high frequency phonons, which is responsible for most of the heat transfer, of bulk crystals, incoherent phonon-phonon umklapp scattering dominates at room temperature. But, by using periodic nanoscale structures such as the dielectric superlattice or periodic porous nanostructured dielectrics such as silicon, some of the high frequency phonon's coherence length can be longer or comparable to the size of the material and coherent heat conduction may be possible. A theoretical investigation using molecular dynamics calculations showed that periodic nanoporous two dimensional silicon structure with a pore sizes less than 1 nm open a phononic band gap and reduce thermal conductivity of crystalline nanostructure to that of amorphous

structure [14]. In another theoretical study by molecular dynamics [15], the authors report a phononic band gap at frequencies greater than 12 THz in a silicon three-dimensional (3D) structure which is made of periodic arrangements of atomic sized silicon isotope cubes. These studies hint at the possibility of coherent phonon scattering for high frequency phonons with the use of periodic nanostructures.

Recently, there are also some experimental reports of partially coherent heat conduction using periodic nanostructures [16 - 19]. Yang *et al.* used a two dimensional holey silicon, on which the sub 100 nm holes were periodically arranged on the silicon sheet and demonstrated a partially coherent heat conduction behavior at low temperatures below 50 Kelvin [16]. A similar study using smaller holes on a two dimensional silicon sheet reported likewise [17]. Luckyanova *et al* [18] have demonstrated using a 12 nm GaAs and 12 nm AlAs superlattice structure that heat conduction below 150 Kelvin behaves in a coherent manner. Most recently, Braun *et al* [19] have shown partially coherent phonon behavior at low temperature in a 3D polycrystalline silicon inverse opal nanostructure (Figure 1.3) with periodicity as small as 400 nm and material thickness of 50 nm.

Periodic nanostructures can demonstrate partially coherent heat conduction at low temperature, but theoretical studies suggest [14,15] such phenomenon can occur at higher temperatures if the periodicity of nanostructures become smaller. To experimentally observe the effects of sub-100 nm nanostructures on partially or fully coherent phonon scattering at higher temperatures, such structures need to be fabricated. This work aims to achieve this goal by describing the fabrication of 3D dielectric inverse opal nanostructure with a periodicity smaller than 100 nm and shell thicknesses on the order of few tens of nanometers.
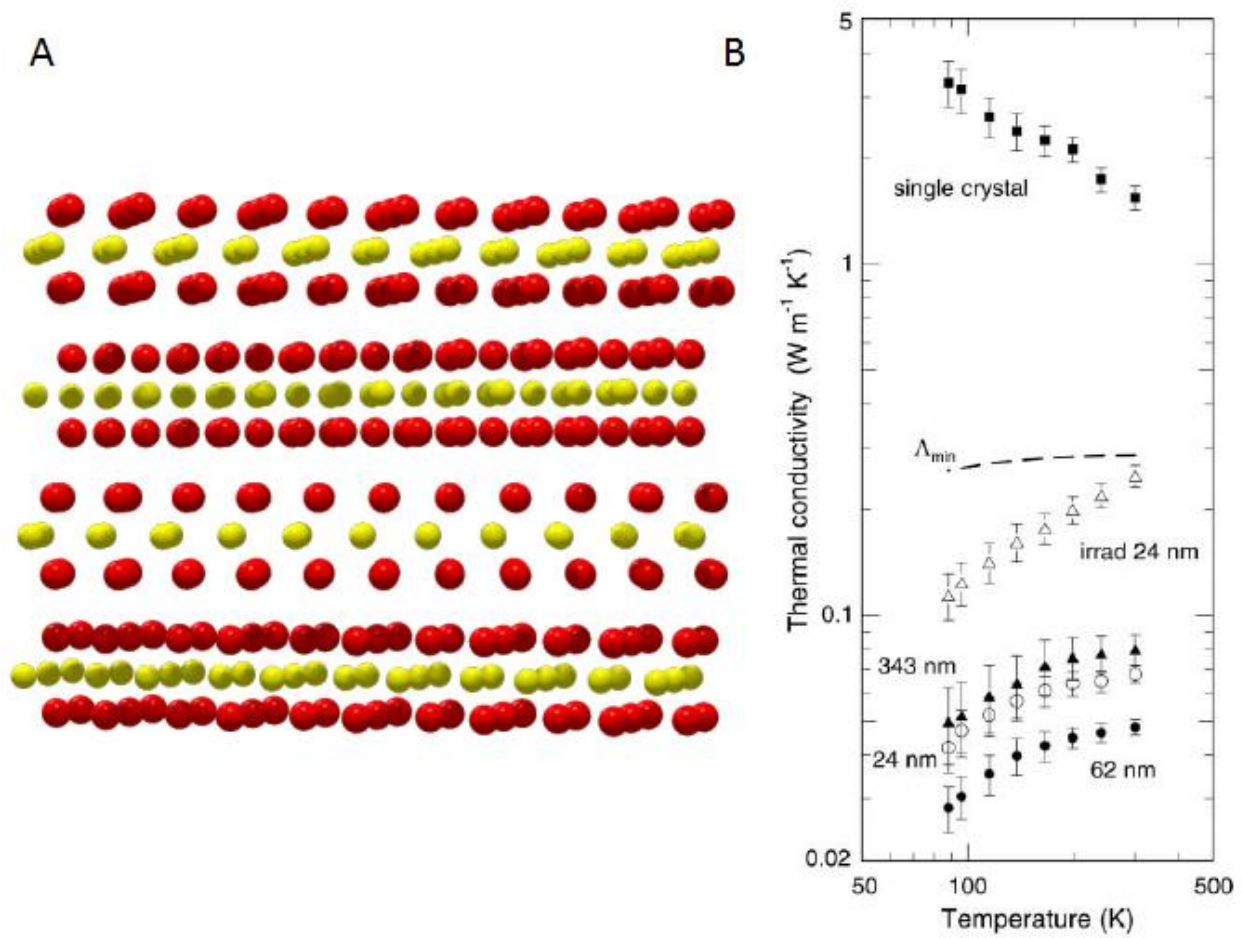
1.3 Figures

Figure 1.1 A) Schematic of WSe$_2$ crystal studied by Chiritescu *et al*. B) Thermal conductivity data reported by Chiritescu *et al*. on the cross-plane of the WSe$_2$ structure. Chiritescu et al. reported thermal conductivity lower than the amorphous limit [6].

4
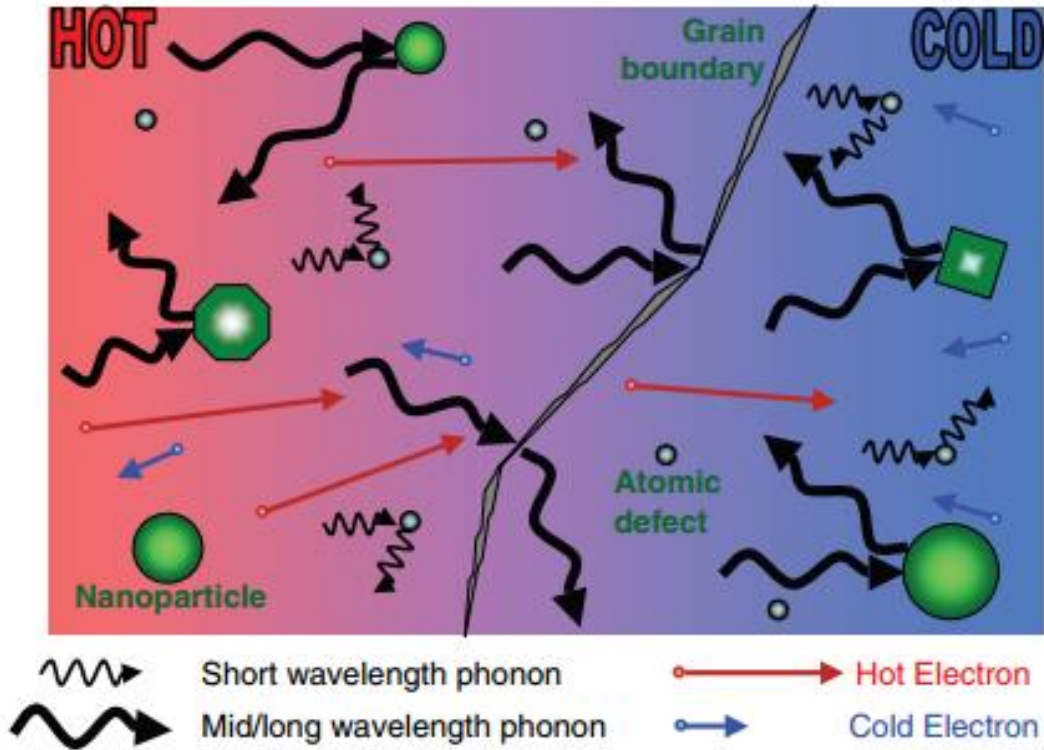
Figure 1.2 Schematic showing how phonons can be scattered within a material. In the presence of defects such as nanoparticles, grain boundary or material boundary, and atomic defects, the phonons can be scattered. Such scattering has found use in lowering the thermal conductivity of the material and has led to a development of more efficient, high figure-of-merit thermoelectric materials [7].
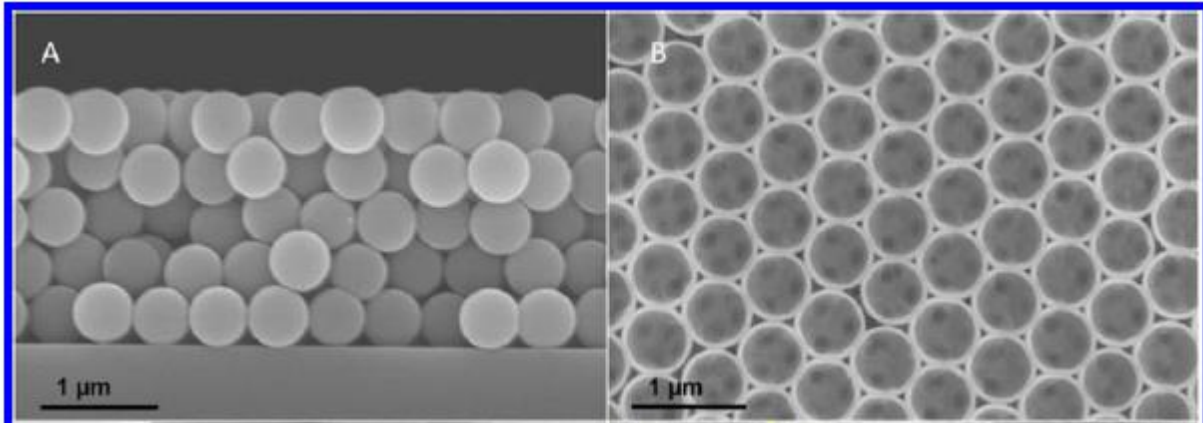
Figure 1.3 Example of an inverse opal structure. Colloidal nanoparticles are stacked in an FCC manner as an opal structure. Dielectric material, in this case Si, is filled into the pores of the structure and the colloidal nanoparticle stacks, opal, are removed via appropriate processing. The remaining structure is the "inverse opal" structure (B). Images were taken from [19].

CHAPTER 2

SUB 100 NANOMETER 3D POLYSILICON INVERSE OPAL NANOSTRUCTURES

2.1 Introduction

Silicon materials are of great interest because of their wide use in electronics and of their well-known fabrication techniques down to the tens of nanometer scale [20]. Silicon materials are widely used to make circuitry, novel 3D multilayer electronics [21], and MEMS (microelectromechanical systems) [22]. These devices are reaching the nanometer scale and a better understanding of the phonon/thermal conduction is needed. Traditionally, Holland's model, which is an approximate analytical solution derived from numerous fitting parameters were used to understand the phonon conduction in silicon [23]. But, as previously mentioned, nanoscale materials can modify the phonon dispersion relation and possible band gap opening can occur. The incongruence of the dispersion with that of the bulk material conditions, from which the model is derived, invalidates the many pre-existing analytical models and necessitates new models for nanoscale silicon materials.

Thus far, thermal studies of 1D, 2D, and 3D nanostructured silicon materials have been reported [8-9, 14-17, 19]. Braun *et al.*'s report [19] particularly draws much interest because most everyday materials are three-dimensional in nature. In this report, the authors utilized the established technique of self-assembly of colloidal particles [24 - 26] to form 3D periodic structures for photonics and used the structures for the thermal study. The structures had shell thickness of ~ 50 nm and were periodically arranged every 400 nm, but the periodicity is still quite large compared to the few tens of nanometers or less used in other reports. The work in this chapter aims to expand the Braun *et al*'s work [19] by using colloidal particles smaller than 100 nm and fabricating sub 100 nm 3D silicon nanostructures.

7

2.2 Fabrication

2.2.1 Synthesis of Silica Nanoparticles

Silicon dioxide (SiO_2), silica, spherical nanoparticles of 80 nm and 40 nm were synthesized using adopted procedures from published procedures by Stöber [27] and Zhao [29]. Glassware was either new or thoroughly cleaned with detergent and a base bath. The glassware was rinsed with deionized water and kept dry in an oven at 60 to 70 $^\circ$C.

Modified Stöber method [27,29] was utilized to prepare silica nanoparticles of 80 nm in size. To a 200 mL round bottom flask, 2.09 g Millipore water (18.2 MΩ resistivity), 3.70 g ammonium hydroxide solution (28 − 30 % NH_3, BDH Aristar Lot#201030472), and 100.0 g of 200 proof ethanol were added and stirred at 700 rpm for 5 minutes. After 5 minutes of mixing, 4.55 g of tetraethyl orthosilicate (TEOS, Sigma-Aldrich Lot BHBV4940) was added to the mixture. The flask was capped and the contents were stirred for 24 hours to allow the reaction to occur. After 24 hours of reaction, roughly spherical SiO_2 nanoparticle seeds of approximately 40 nm formed (Figure 2.1). To enhance the roundness of the particles by growing the seeds slightly, seeded growth of SiO_2 was performed by adding one-third of the initial reactant amounts every 24 hours. Generally after 5 seeded growth, the size of the silica nanoparticles increased to 80 nm ± 10 nm.

Once the target size was reached, the mixture was transferred to 50 mL centrifuge tubes. The mixture was centrifuged at 10000 rpm for 15 minutes and the resulting supernatant was slowly poured out as waste. Afterwards, the settled particles were re-dispersed in 30 mL of ethanol via sonication for further centrifugation. The above process was generally repeated 5 times and the solution was dried on the hot plate overnight to obtain nanoparticles. In order to

avoid cracking of the opal structure during high temperature postprocessing [30], the particles (Figure 2.2) were heat treated at 600°C for 10 hours prior to storing in a clean vial.

Silica nanoparticles of 40 nm were prepared via reverse micro-emulsion method [28]. To a 500 mL round bottom flask, 44.43 g of Triton X-100 (Fluka, Lot 1209067), 146.20 g cyclohexane (Sigma-Aldrich, >99%, Spec grade, Batch#11966BE), and 32.34 g 1-hexanol (Acros, 98% pure, Lot A0308579) were added and stirred for 30 minutes at 800 rpm. Once the mixture was mixed thoroughly, 10.01 g of Millipore water was added and stirred for additional 5 minutes. Afterwards, 1.27 g of ammonium hydroxide solution (28 − 30% NH_3) was added and stirred for 5 minutes. Finally, 2.29 g of TEOS was added to the mixture. The mixture was capped and left stirred for 24 hours. After 24 hours, the nanoparticles could be obtained. 200 mL of ethanol was added to the mixture after the stirring was stopped. Within 1 hour of the addition of ethanol, ethanol and the oil mixture phase-separated and the silica nanoparticles settled to the bottom along with ethanol. Using a Pasteur pipette, precipitated silica nanoparticles of approximately 30 to 40 nm were transferred to 50 mL centrifuge tubes.

Immediately after the transfer, silica nanoparticles were surrounded by large amounts of surfactant, Triton X-100, used in the reaction (Figure 2.3) and needed to be cleaned. The colloid mixture was first centrifuged at 10000 rpm for 30 minutes and the resulting supernatant was removed as waste. The particles were re-dispersed in ethanol via sonication and dialysis was performed to remove the surfactant. In the first dialysis, the colloid solution was dialyzed against ethanol for 24 hours. Afterwards, the mixture was dialyzed against 1 L Millipore water bath and the water was exchanged daily for 3 weeks. After the dialysis, the colloid mixture was dried in 60 − 70 $^{\circ}$C oven overnight prior to the calcination of the nanoparticles at 600 $^{\circ}$C for 10 hours to

remove the remaining organic residue (Figure 2.4). After the calcination, the nanoparticles were stored in glass vial for further use.

2.2.2. Silicon Inverse Opal

Using the synthesized silica nanoparticles above, colloidal crystal film was self-assembled into an opal structure on a single side polished Si (100) wafer. The silicon wafer was cut into 1 cm by 3 cm size and cleaned using a Piranha solution (3:1 H_2SO_4:H_2O_2) and rinsed with Millipore water. After the rinse, each substrate was placed at a 30° angle in a 20 mL scintillation vial containing a colloidal solution of 5 mg of particles in 0.8 g of ethanol using a modified vertical deposition method [31] (Figure 2.5). The vials were left in an incubator (Fisher, Isotemp 125D) at 37.0 $^{\circ}$C until all the solvent had evaporated.

After the silica particles self-assembled into an opal structure templates (Figure 2.6A, 2.7A), the opal templates were deposited with silicon. The templates were only completely filled with amorphous silicon when using a custom-built static chemical vapor deposition (CVD) system with disilane (Si_2H_6, Gelest, 98%). Growth via commercial low-pressure chemical vapor deposition (LPCVD) system (Firstnano Easy Tube LPCVD, 200 mTorr, ~560 $^{\circ}$C) was attempted, but silicon deposited on the top of the opal structure and failed to infiltrate the pores (Figure 2.8). When static CVD growth conditions of base pressure of ~6.0E-5 mbar, disilane pressure of 50 mbar [B6], 8 $^{\circ}$C per minute heating rate to 350 $^{\circ}$C, and a dwelling time of 3 hours at 350 $^{\circ}$C were used, silicon deposited inside the pores of the opal structure (Figures 2.6B, 2.7B).

Once removed from the CVD reactor, silicon-opal samples were placed on top of alumina crucible, were inserted into a quartz tube, and were annealed at 1000 $^{\circ}$C for 10 hours under forming gas environment (95% Ar, 5% H_2). Post-annealed silicon structure underwent

reactive ion etching (3 min, 50 mTorr, 70 W, 19 sccm SF_6 and O_2 each) to open a small window on top of the structure defined by Kapton film to expose the opal structure (Figure 2.6C, 2.7C). The exposed structure was submerged in 5% hydrofluoric acid solution (85% water, 10% ethanol, 5% HF) for 75 minutes to completely etch the silica nanoparticles away without damaging the silicon inverse opal structure. (Figure 2.6D, 2.7D)

2.3 Characterization of Silicon Inverse Opal

The 80 nm and 40 nm silicon inverse opal material properties were characterized by x-ray diffraction (XRD) and transmission electron microscopy (TEM). Due to the fragile nature of the nanostructure, XRD and TEM analysis were performed prior to the HF etching. For the XRD analysis (Panalytical / Philips X'Pert™ MRD System, Cu K-alpha, 0.15418 nm), glancing angle method which utilizes an incoming x-ray beam of 1° relative to the surface of the sample was used due to the low amounts silicon present in the thin porous structure to enhance the signal. XRD analysis revealed the amorphous silicon recrystallized to polycrystalline silicon after annealing at $1000\ ^{\circ}C$ (Figure 2.9). Grain sizes in the polysilicon inverse opal were analyzed using the Scherrer equation:

$$\tau = K\lambda\ /\ \beta\ \cos\theta \qquad (1)$$

where τ is the grain size, K is a shape factor, λ is wavelength of the x-ray, β is line broadening at half the maximum intensity, and θ is the Bragg angle. The analysis revealed average silicon grain sizes, found by averaging the three grain sizes from the three silicon orientation peaks, for both 80 nm and 40 nm to be around 9 nm (Figure 2.9).

To confirm the analysis of the data obtained glancing angle XRD, cross-sectional high resolution TEM (Figure 2.10) was employed as an additional analytical tool. TEM sample was

prepared by grinding the sample and ion milling. Selected area electron diffraction on the inverse

opal structure confirmed the polycrystalline nature of the silicon inverse opal and high resolution

TEM showed typical silicon crystal domain sizes to be on the order of the size analyzed by XRD.

2.4 Future Directions/ Thermal Conductivity Measurement

Using the silicon inverse opal structure, accurate thermal transport study should be

performed in the future. There are two primary methods which thermal transport can be studied

by measuring thermal conductivity: 3-omega method [32] and time-domain thermoreflectance

(TDTR) [33]. 3-omega method utilizes a metal heater on top of the structure where an AC

current at frequency omega is used to generate a heat flow at 2ω which gives the resistance

change in the heater due to the temperature fluctuation. By measuring the voltage at 3ω, the

temperature fluctuation is extracted at 2ω using the information from the input AC current to

derive the thermal property of the sample. TDTR is a pump-probe laser method which measures

the thermal property based on the change in reflectivity of the surface, usually a metal transducer

layer with known optical property, which arises from the temperature dependence of the optical

constants. Utilizing either of the two techniques, accurate thermal transport study on the

nanostructure is needed.

A few attempts to study the thermal transport on the structure have been made, but to no

avail. TDTR can measure at picosecond intervals and attempts at TDTR were made first.

Conventional TDTR measurement by simple aluminum metal deposition on top of the opal

structure proved to be difficult due to the roughness on top of the surface (Figure 2.11). Low

magnitudes of the signal around 10 µV compared to the typical 150 µV in flat silicon substrates

were recorded when the measurements could be made, which decreased the signal-to-noise ratio

greatly.   Since signal-to-noise ratio could be improved using a flatter surface, attempts to measure from the backside of the structure was made by flipping the structure using a schematic outlined in Figure 2.12.   However, too much damage on the structure occurred during the process (Figure 2.13); thus, 3-omega is the preferred method of measurement and should be pursued in the future.

Several attempts were made to prepare the 3-omega measurement sample by bonding the gold wire to the deposited metal heater on top of the silicon inverse structure. However, the fragility of the structure and a poor adhesion between the silicon substrate and the inverse opal structure, which may have occurred during the HF etching process, caused problems with the preparation of the 3-omega sample. It has been unsuccessful thus far because the wire bonding process applies a large amount of drag force on the structure. To resolve the problem of interfacial adhesion between the substrate and the inverse opal, pre-depositing silicon before the opal growth may protect the delamination of interface during the HF etch. Also performing HF etch prior to the opal assembly may help the adhesion because hydrogen terminated surface will be exposed up and stable for hours [34] after the removal of the native oxide layer with HF and such areas could potentially serve as strong silicon − silicon bonding points that resist the HF opal removal step. With this, preparation of 3-omega samples could be improved for the study of thermal transport.

Another interesting project which could utilize the above structure could be to research into the use of a thermoelectric device. One and two dimensional silicon nanostructures have been widely studied as a potential thermoelectric material [8, 9, 16]. Thermoelectric device is better in three dimensions because the current is collected in the plane perpendicular to the plane of thermal gradient, so improved devices can be made. Furthermore, doping of silicon is a well-

known processing technique in the semiconductor industry. Different levels of doping can be investigated and can be compared against reported theoretical calculations [35].

2.5 Conclusion and Final Remarks

Using self-assembly of sub-100 nm silica nanoparticles, sub-100 nm polysilicon inverse opals were successfully fabricated. Attempts to study the thermal transport utilizing TDTR had problems and 3-omega should be used to study the thermal transport of the structure in the future with modifications to strengthen the structure.

2.6 Figures
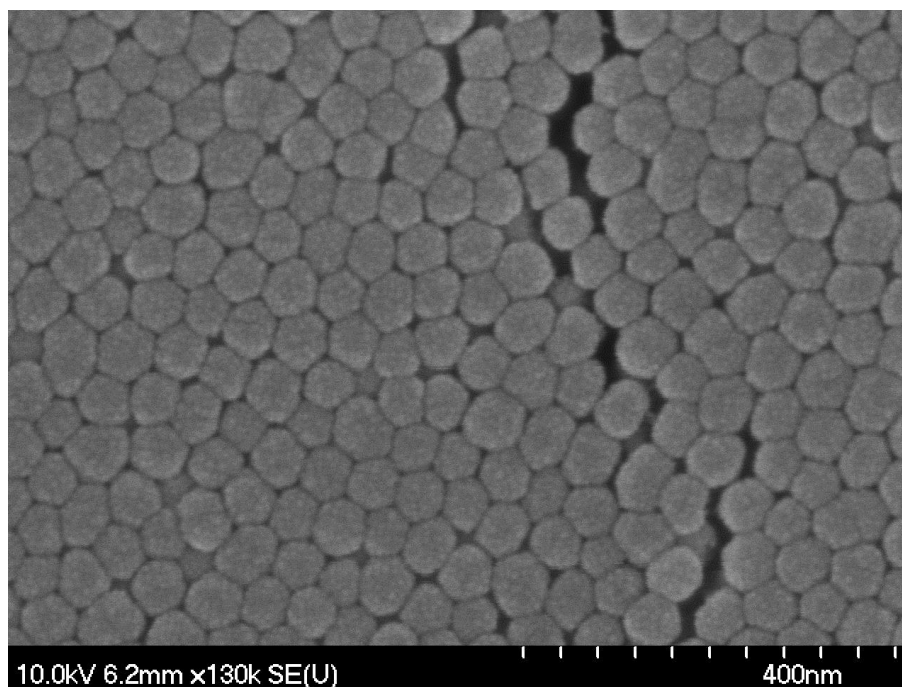
Figure 2.1. Scanning electron microscopy (SEM) image of initially formed SiO_2 nanoparticle seeds after 24 hours of reaction.
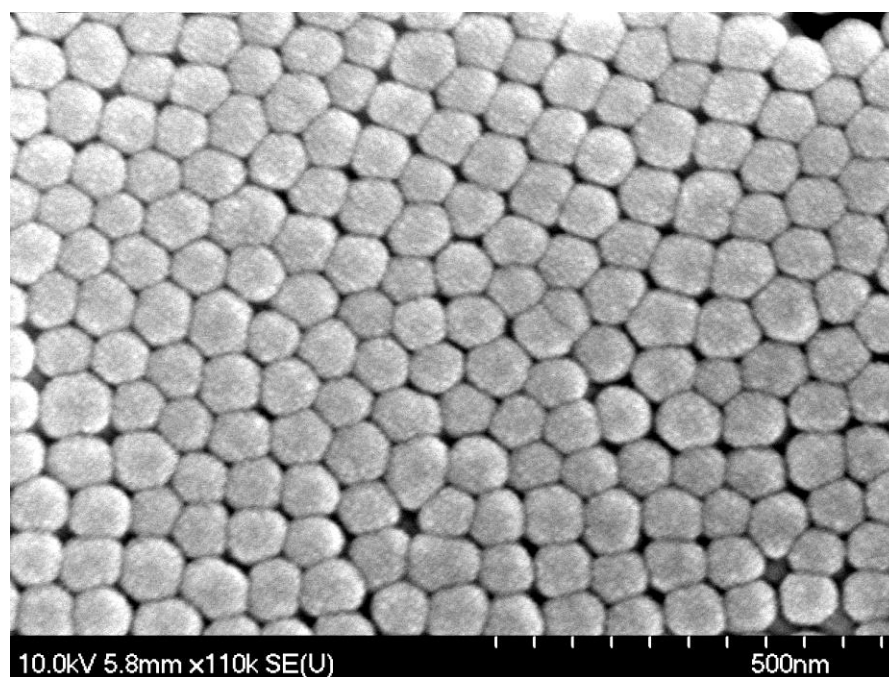

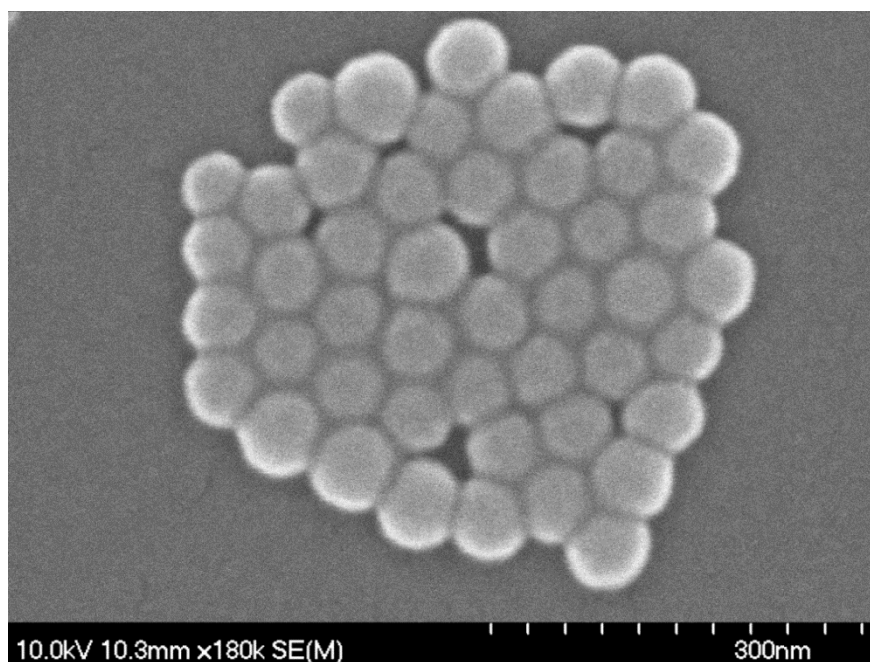Figure 2.2. SEM Image of SiO_2 nanoparticles after seeded growth.

15

Figure 2.3. SEM image of SiO$_2$ nanoparticles prepared via reverse microemulsion method prior to cleaning of the particles. Between the particles, surfactants are present.
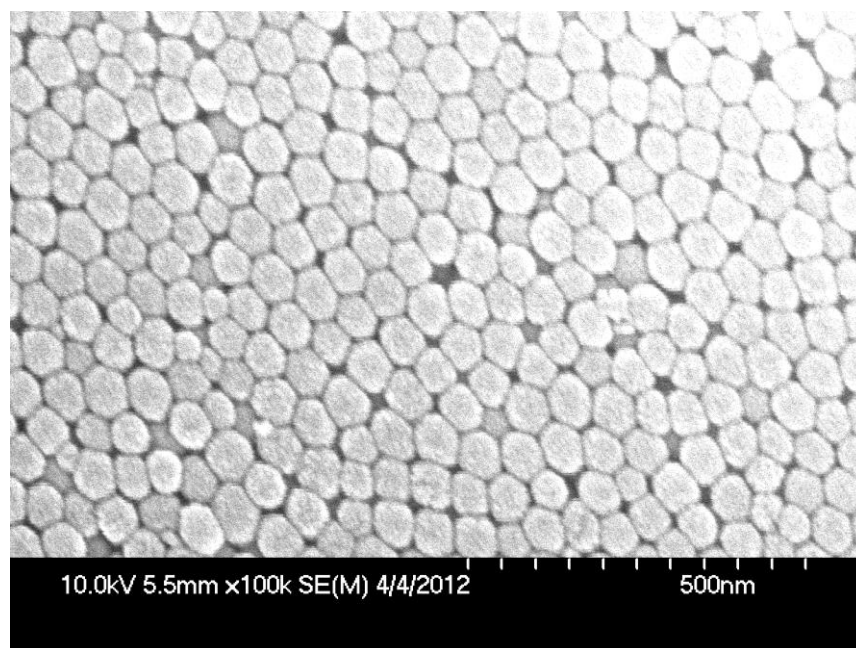

Figure 2.4. SEM image of SiO$_2$ nanoparticles prepared via reverse microemulsion method after dialysis. The surfactants which used to be present in between the particles are no longer present.
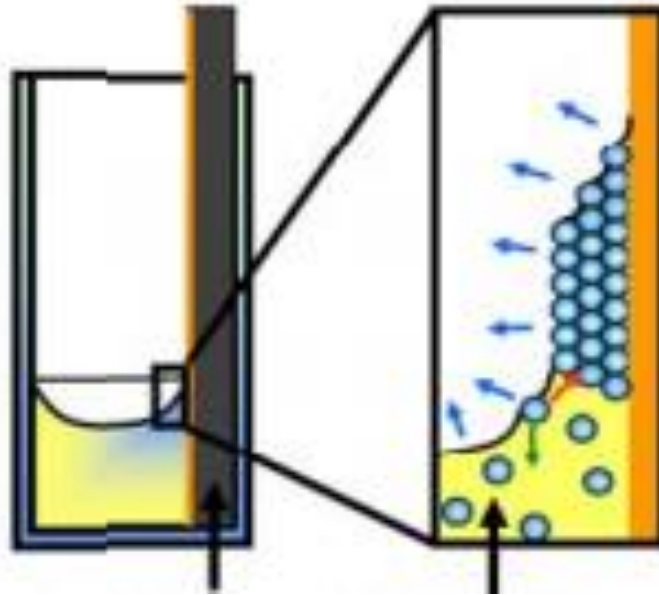
Figure 2.5. Schematic of opal structure assembly from colloidal particles. The substrate is submerged in a colloidal solution and as the solvent evaporates, the colloidal particles self-assemble on top of the substrate. Figure was taken form [26].
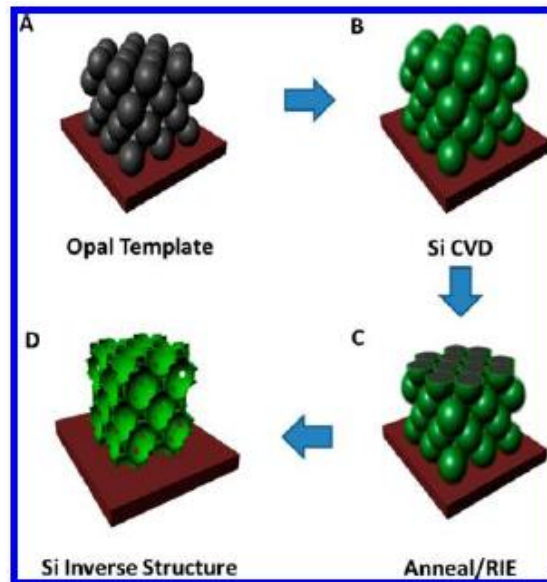

Figure 2.6. Silicon inverse opal fabrication schematic [19]. A) SiO_2 opal structure is self-assembled from colloidal suspension. B) Static silicon CVD is performed. C) Top portion of the structure is exposed via reactive ion etching. D) Using dilute HF solution, silica particles are etched away. Silicon inverse structure remains on the substrate.
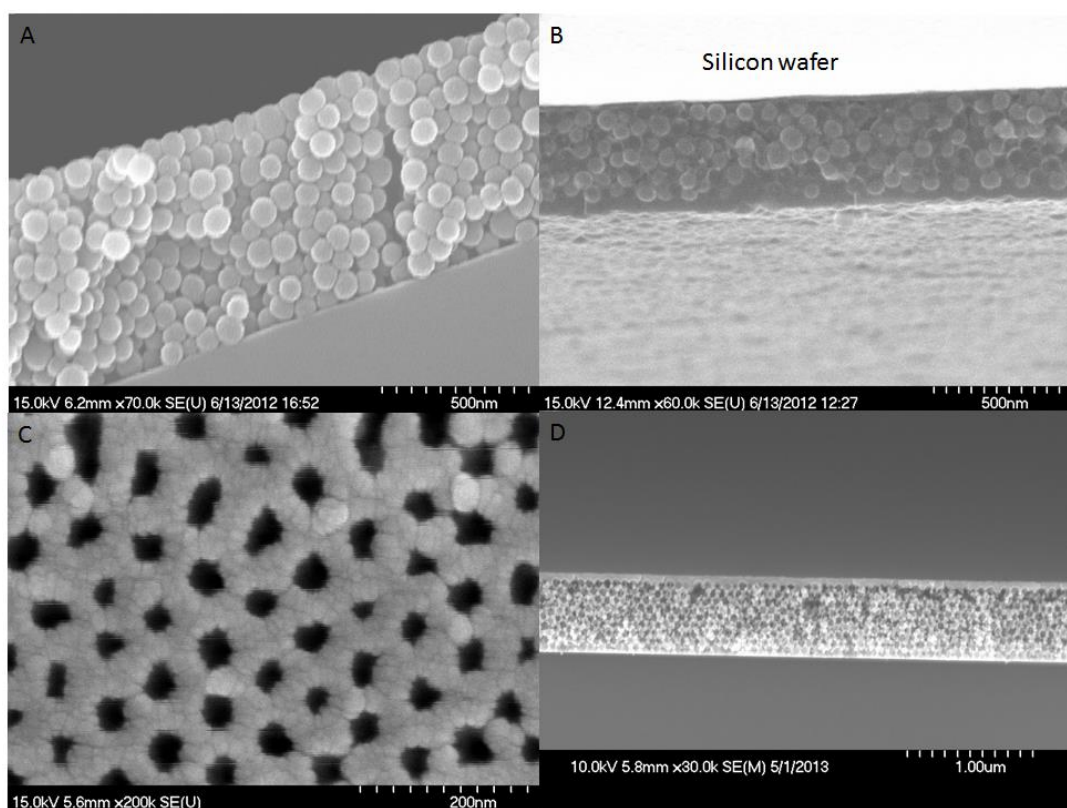
Figure 2.7. SEM images illustrating Figure 2.6. A) Cross-sectional view of the opal template after the colloidal self-assembly. B) Cross-sectional view of silicon deposition into the opal structure. C) Top view of the structure after opening a window with reactive ion etching and dilute HF etch. D) Cross-sectional view of the silicon inverse opal structure.
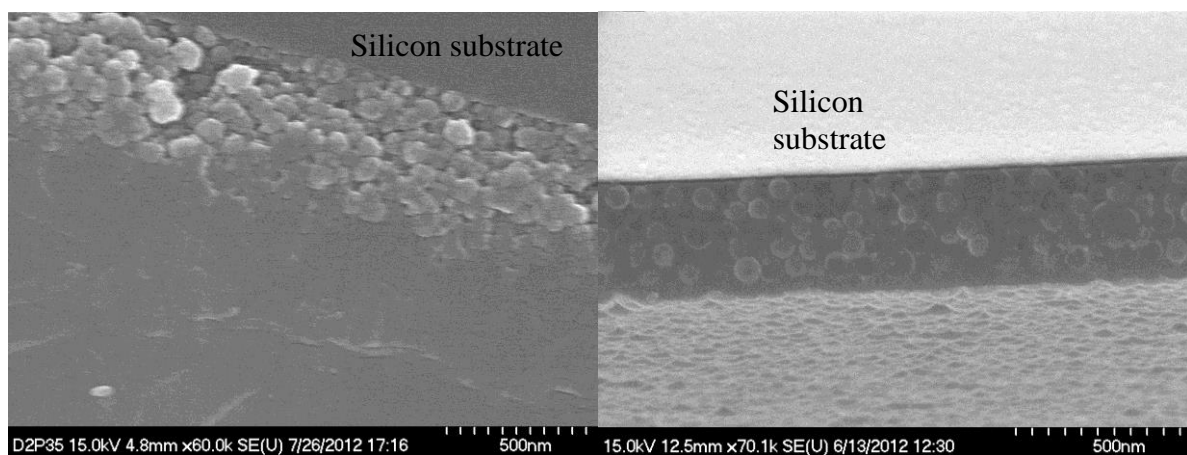

Figure 2.8. SEM image of silicon deposition into 80 nm SiO_2 particle opal structure. Amorphous silicon is deposited using LPCVD (Left) and static CVD (Right). LPCVD shows some void space near the opal silicon substrate interface (top of the left image) while the static CVD does not (top of the right image).
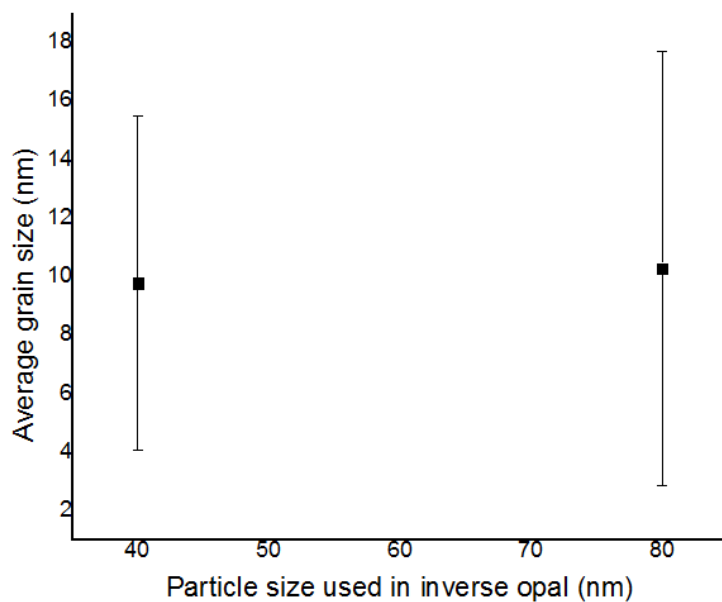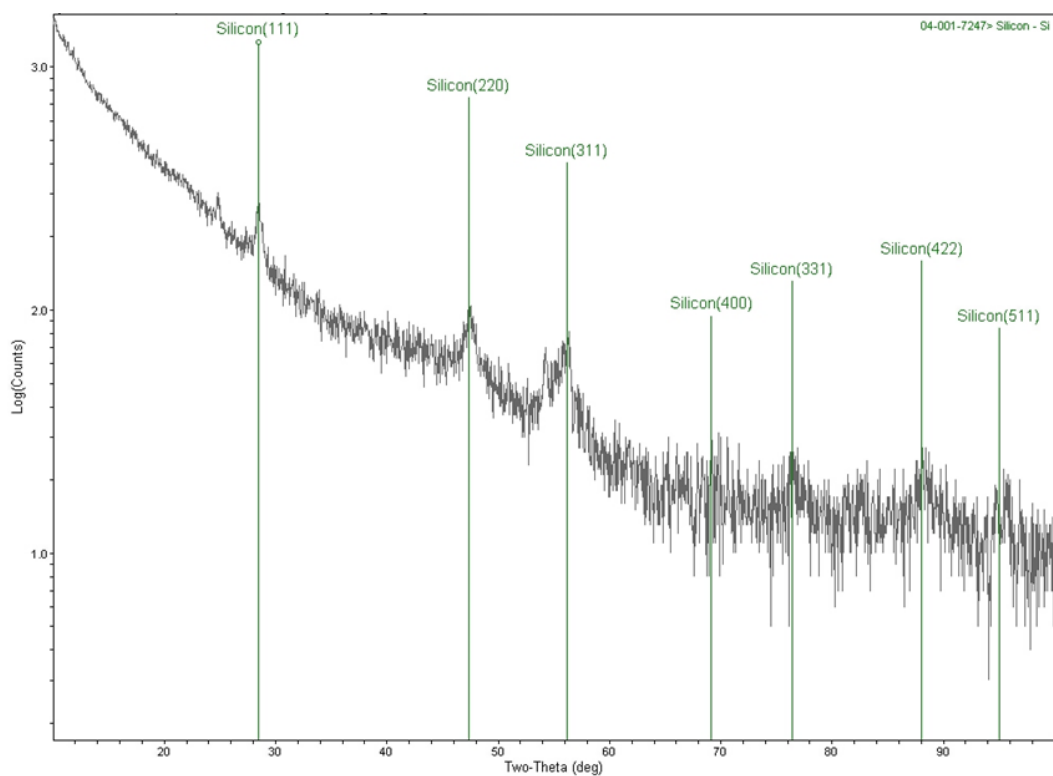
Figure 2.9. Typical x-ray diffraction (XRD) profile of the 40 nm or the 80 nm silicon inverse opal (TOP). Peaks of silicon show the polycrystalline nature of the structure. Grain size analysis was performed on the XRD profile using Scherrer equation and average grain size were obtained by averaging the grain sizes of 3 orientations for 4 different samples made at each size.
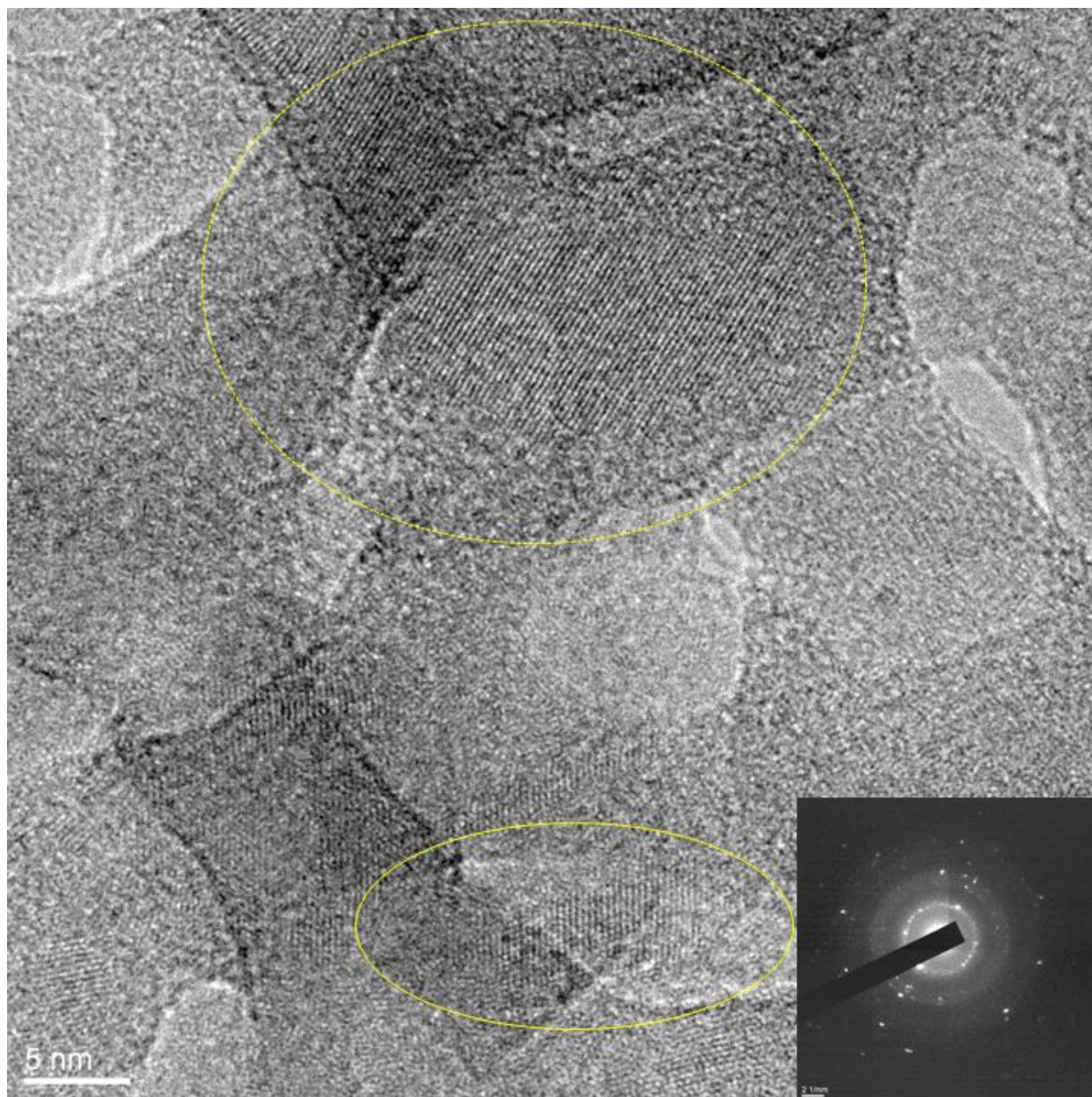
Figure 2.10.   High Resolution TEM image of the silicon inverse opal with the silica particles remaining intact. Large spherical shapes are the SiO_2 nanoparticles. Yellow circles show two different orientations of the lattice orientation of silicon in the opal structure. The rough grain sizes of each orientation are on the order of the size shown by XRD. The inset, selected area electron diffraction pattern, confirms the polycrystalline nature of the silicon in the opal structure.

Figure 2.11 Aluminum transducer layer was sputtered on top of the silicon inverse opal structure. Compared to the flat silicon substrate area near the tweezer, the silicon inverse opal region shows a dull color and was unable to reflect the light well.
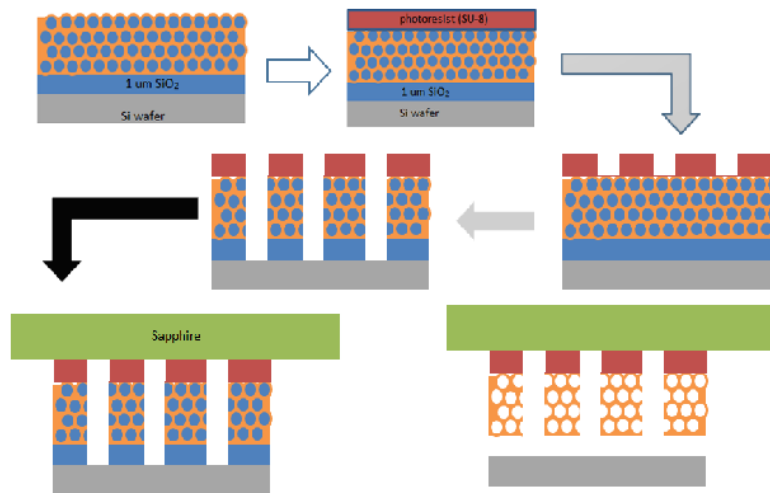

Figure 2.12 Schematic of the flipping procedure (developed by labmate H. Ning) to attempt TDTR from backside of the structure. In the first step silicon inverse opals were fabricated on a substrate with a 1 micron SiO_2 layer. SU-8 photoresist was spin coated using 1000rpm for 5 seconds and 2000 rpm for 40 seconds. SU-8 was pre-baked at 110^oC before using a Karl Suss Mask Aligner to pattern via lithography. The photoresist was developed and hard baked at 125^oC. Using 12:6:1 HNO_3:HF:H_2O etch for 2 minutes, the structure was etched in the un-patterned area. Using a sapphire substrate on polydimethysiloxane the structure was attached to the photoresist using Norland Optical 61 by curing for 5 minutes with UV light. Aftewards, the 1 micron SiO_2 layer was etched with the nanoparticles to detach the substrate.
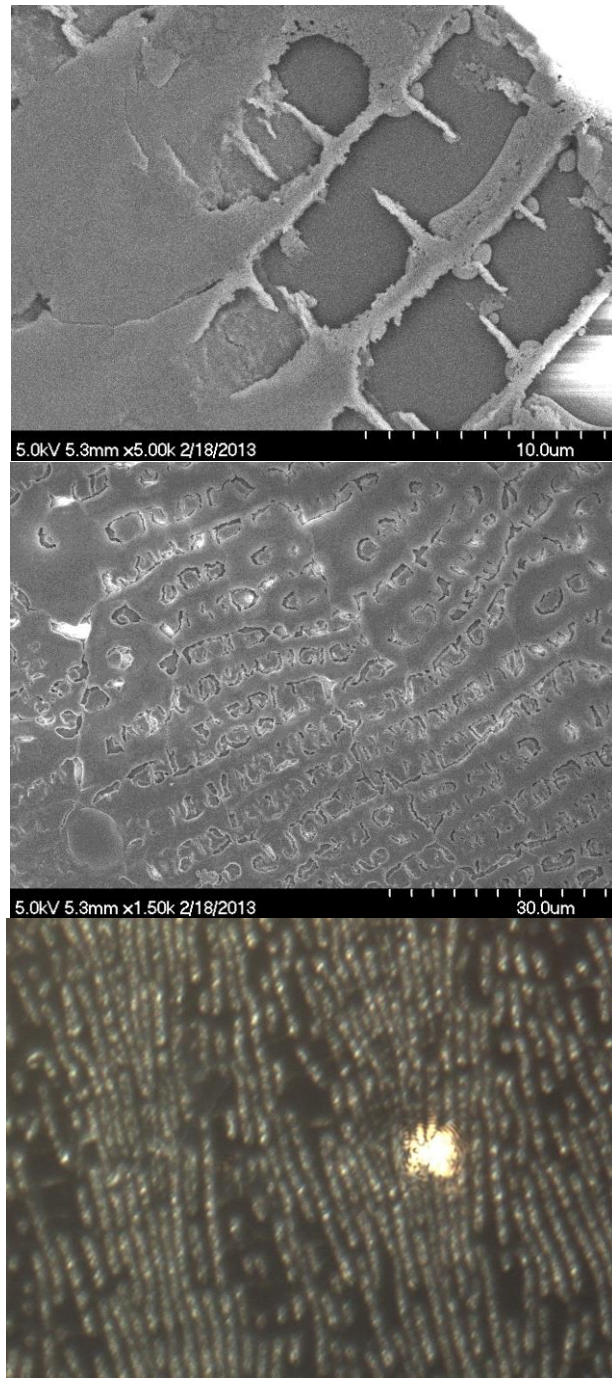
Figure 2.13 SEM images (TOP 2) and a microscope image (bottom) showing the top surface of the flipped silicon inverse opal using the procedure outlined in Figure 2.12. Because of the thin silicon structure at the bottom, the surface is rough due to the silicon etching and no useful area which the TDTR laser with a beam size of $1/e^2$ radii of 8 μm can hit on the smooth area can be found.

CHAPTER 3

ELECTRODEPOSITION OF EPITAXIAL CUPROUS OXIDE INVERSE OPAL STRUCTURE

3.1 Introduction

Polycrystalline sub 100 nm silicon inverse opals fabricated in Chapter 2 can provide interesting structures to study nanoscale phonon conduction, but it still do not present with the ideal structure for thermal studies. The primary drawback of the silicon inverse structure resides with the polycrystalline nature of the material as the grain boundaries within the structure provide sites for the phonon – grain boundary scattering. These grains cannot be controlled in a periodic manner, so single-crystal or epitaxial nanostructured material would be better for nanoscale thermal study. A second drawback is that the CVD grown silicon may have significant hydrogen doping and thus a high concentration of point defects.

The growth of single-crystal or epitaxial materials are generally done using crystallization from a melt, e.g. the Czochralski process, or using chemical vapor deposition (CVD) [36-39], but it can also be done electrochemically[40-43]. Electrodeposition offers advantages compared to CVD based methods. Certain CVD based methods tend to have terrible infilling of the 3D opal template and deposit only on the top few layers of the opal. Braun and Wiltzius have shown electrodeposition circumvents incomplete filling problem and completely deposits within the pores of the opal [44]. Electrodeposition also tends to have a more rapid deposition rates than vapor based methods. In this chapter, efforts were made to combine the two approaches and fabricate epitaxial dielectric inverse opal nanostructures.

3.2 Cuprous Oxide

Of the limited choices of materials that can be electrodeposited epitaxially, cuprous oxide (Cu_2O) was chosen as the material of choice. Cuprous oxide is a semiconducting material with a band gap of 2.1 eV and is easily processed via thermal oxidation of copper for mass production at low cost [45]. Due to its photovoltaic properties, it has a promising application as solar cell material. Furthermore, Cu_2O exhibits a good thermoelectric effect and can be potentially doped to form efficient thermoelectric device with the figure of merit value of 0.6, which is a high value compared to the value of 1 -2 found in the world's best thermoelectric devices [46]. For its wide applications, Cu_2O was chosen as the material of investigation. To fabricate the structure, methods were adopted from Switzer's report [47].

3.3 Electrodeposition of Epitaxial Cu_2O Inverse Opal

Following the procedures in Switzer's paper [47], epitaxial Cu_2O film was deposited. In the first step, the deposition electrolyte was prepared. To a 200 mL glass bottle, approximately 75 grams of 85% lactic acid solution (Sigma Aldrich, Lot KMBK2646V) was poured. Afterwards, Millipore water was poured until the 150 mL mark. The bottle containing the acidic solution was submerged into an ice bath and approximately 17.5 grams of sodium hydroxide (Fisher Scientific) was slowly added while the solution was carefully stirred. The solution was left in the ice bath to cool the heat released from the exothermic reaction of acid and base and returned to room temperature. 20.0 grams of copper sulfate pentahydrate ($CuSO_4 \cdot 5H_2O$, Fisher Scientific, Lot 110549) was added prior to adding additional Millipore water until a total volume of 200 mL was reached to make 0.4 M Cu^{2+} and 3 M lactate ion solution.

A 100 mL portion of the above electrolyte transferred to a three-electrode cell to deposit Cu_2O film. The electrolyte was placed a custom made cell (Figure 3.1) and the cell was

24

submerged into a silicone oil bath to heat the solution to 65 $^\omega$C. Using a pre-made 1 M NaOH solution or lactic acid solution, pH was re-adjusted to 9 at 65 $^\circ$C before the deposition. The cell was capped and sealed with Parafilm to avoid evaporation of the solution. A 1cm by 3 cm p-type single crystal silicon (100) wafers (WRS Materials, 0.005 – 0.025 Ω cm resistivity) which were treated with 1 minute dip in 5% hydrofluoric acid (HF), 15 minutes dip boiling Millipore water, and another 5% HF dip for 20 seconds prior to submerging the substrate in the 65 $^\circ$C electrolyte for a minute were used as the working electrode. Silicon wafers were treated in the above manner to etch away the native oxide layer and expose the silicon so that the Cu^{2+} ions are reduced by the silicon to produce epitaxial Cu_2O seeds (Figure 3.2) [47]. Standard calomel electrode (SCE) was as the reference electrode and a platinum foil was used as the counter electrode. A potential of -0.45 V against the reference electrode was applied to deposit epitaxial Cu_2O.

The deposited Cu_2O films had aligned squares and pyramids covering the surface of the silicon (Figure 3.3) similar to the images reported by Switzer [47] as shown by the scanning electron microscopy (SEM). X-ray analysis of the film were performed by taking omega – 2theta scans and pole figures from (111), (200), (220) directions of Cu_2O were taken on X'pert (Philips X'pert MRD system). Details of x-ray analysis will be in the next section. After the x-ray analysis, 400 nm silica opal structures were self-assembled on top of the Cu_2O film as described in Chapter 2 using 1 mL of 3% Stöber silica nanoparticles by weight colloidal suspension in ethanol. After the opal assembly, the prepared substrate is once again submerged in the electrolyte at 65 $^\circ$C and -0.45 V versus SCE is applied for further deposition of Cu_2O. SEM shows that Cu_2O is successfully filled inside the opal structure (Figure 3.4). Afterwards, x-ray analysis of the above is performed again.

3.4 X-ray Analysis of the Structure

X-ray diffraction (XRD) pattern (Figure 3.5) of the as deposited film suggests the epitaxial nature of the Cu_2O film as reported by Switzer [47]. Aside from the (004) peak of the silicon wafer used, XRD pattern shows two peaks which correspond to the (002) and the (004) orientation of the Cu_2O. The XRD pattern was checked against copper (II) oxide (CuO), another form of copper oxide, XRD database (Figure 3.5), to ensure Cu_2O was the material being deposited rather than CuO. The appearance of the single family of XRD peak implies that the grains of the film are grown in the (001) direction of the Cu_2O crystal and the film is either strongly textured or epitaxial in nature. To verify the epitaxial nature of the crystal, pole figures were taken from the (111), and (220) orientation of the Cu_2O.

Pole figures (Figures 3.6 -3.7) strongly suggest the epitaxial nature of the Cu_2O film. A pole figure is an x-ray analysis technique in which the planes corresponding to different crystal orientation are probed by selecting a specific Bragg angle, θ, and then the sample is tilted at a series of angles, ψ, in $5°$ intervals for this thesis. At each ψ, the sample is then rotated through the entire $360°$ of the azimuthal angle, φ. When the Bragg condition is met, the peaks will appear. In the case of a strongly textured film, the pole figures will display a ring at a specific tilt angle corresponding to the family of peaks when the Bragg condition is met since there is no orientation in the plane of the crystal. However, in the pole figures there is no ring, but four sharp points at specific tilt angles, which indicates the presence of in-plane orientation of the film. The appearances of four sharp symmetric points indicate 4-point symmetry of the crystal in the plane. Cu_2O is known to have a cubic structure, which supports the fact that the crystal is Cu_2O. In the pole figures taken from the (111) and (220) orientation of the Cu_2O, it was found that the

26

maximum peak occurred at $\psi = 55°$ and $45°$ respectively. Using simple geometry of vectors, the predicted ψ values of peaks can be calculated in the following manner:

$$Cos (\psi) = (u_1\ v_1\ w_1) \cdot (u2\ v2\ w2) / \|v_1\|\ \|v_2\|$$

where $(u_1\ v_1\ w_1)$ and $(u_2\ v_2\ w_2)$ are x,y, and z coordinates of vectors v_1 and v_2 and the vectors represent the crystal orientation at which the Bragg angle, θ, was fixed and the crystal orientation of interest respectively. For the (200) peaks of Cu_2O, $\psi = 54.7°$ and $45°$ from the (111) and the (220) orientation respectively, so the pole figures confirmed that Cu_2O film grew in the (200) direction epitaxial as reported by Switzer [47].

After the opal assembly and infilling of the opal, XRD was taken. Thus far, I have tried to avoid over-deposition of Cu_2O by controlling the deposition time. Furthermore, I have utilized only thick Cu_2O films to grow the opal as shown in Figure 3.4 thus far. Consequently, only a very small change in the XRD pattern was noticed (Figure 3.8) because the amount of the extra material deposited in the opals were minute amounts relative to the Cu_2O present within the film. The intensity of the silicon peak decreased while the intensity of the Cu_2O remained constant, which could imply that a slight increase of Cu_2O film amount was detected via x-ray due to the increase of the ratio of Cu2O (002) to silicon (004) increased from 10.69 to 13.45. Also, the fact that the other orientations of Cu_2O did not appear during this process could suggest that Cu_2O experienced epitaxial growth inside the opal as suggested by a pole figure from (111) orientation (Figure 3.9).

Another note that can be on the epitaxial suggestive film that was grown. The full width half maximum of the Cu_2O (002) and the Si (004) from the XRD pattern was compared. Cu_2O films demonstrated a range of values of $0.8°$ to $2°$ while the Si (004) had a value of $0.6°$. This implied that the Cu_2O film had a slight "mosaic spread" where the crystal has a near perfect

bonding with the substrate rather than the ideal case when the film is epitaxy (Figure 3.10). Depending on the film sample, the degree of mosaic spread varied.

3.5 Discussion and Future Direction

Using the x-ray analysis, Switzer's work [47] was successfully replicated and extended into the growth of an opal. However, the analysis via x-ray is incomplete because the opal layer was too thin compared to that of the initial film. For a more complete analysis, the initial film of Cu_2O needs to be much thinner than the opal layer so that the information from the opal structure may be obtained. From current knowledge, the Cu_2O that infiltrated the opal structure is highly suggestive of epitaxy, but further investigation using a transmission electron microscopy (TEM) is needed to confirm the epitaxy nature of the structure. To confirm, select area diffraction pattern on the opal structure as well as high resolution TEM image showing the lattices near the opal structure are needed. Also, to confirm Switzer's work, high resolution TEM image is also needed on the interface of silicon and Cu_2O since it has been checked via x-ray analysis only.

Aside from the need to verify the epitaxial nature of the crystal via another method, Cu_2O structure should be used to study nanoscale thermal transport. Thermal transport could be studied in 400 nm inverse opal Cu_2O structures, but the size of the necks in such structures is on the order of 100 nanometers, which is too large to see many interesting thermal transport phenomena such as high frequency phonon band gap. Thus, deposition of Cu_2O epitaxially into the sub 100 nanometer structures is needed. Additionally, a method to create an air void space is needed. If the silica nanoparticles are left inside the structure, such sites could provide additional umklapp scattering sites which would affect the thermal transport. Silica can be typically etched away using a 25 minutes dip in 5% ethanolic HF solution [19], but this procedure is unsuitable

for Cu_2O. As a simple test, Cu_2O film was dipped into 5% ethanolic HF solution, but the film delaminated and dissolved away because dilute HF can etch away oxides including copper oxides [48]. Alternative silica etching processes without damaging the silica nanoparticles or alternative opal systems need to be investigated.

However, preliminary investigation with polystyrene system, an alternative opal structure that can be removed using an organic solvent such as tetrahydrofuran without damaging the oxide, does not look promising. The oxide is unable to deposit and the energy dispersive x-ray spectroscopy (EDS) show that carbon junk infills and clogs the opal structure instead (Figure 3.11 and 3.12). Few more attempts must be made to clarify the problem, but a different opal system other than polystyrene may be necessary for the thermal study.

Lastly, using the above structure, interesting applications into photonic crystals and thermoelectric can be investigated. Nelson *et* al. [39] used epitaxial three-dimensional gallium arsenide (GaAs) opal structure to create an optoelectronic device and epitaxial Cu_2O could provide optoelectronic device with different property from that of GaAs. Cu_2O has shown to have thermoelectric properties as mentioned before, and nanostructured epitaxial Cu_2O could prove to be an ideal material for cheap, efficient thermoelectric device.

3.6 Conclusion

Following Switzer's recipe on epitaxial Cu_2O, Cu_2O has been deposited into 400 nm silica opal structure successfully. Initial x-ray analysis strongly suggest epitaxial nature of the Cu_2O, but further investigation such as TEM and careful designing of the materials for a new x-ray analysis are needed.
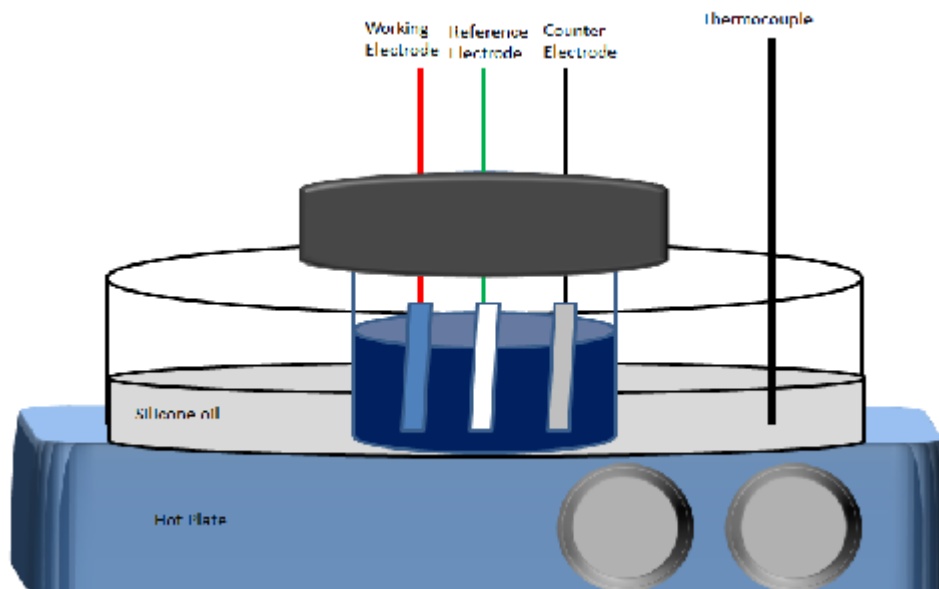
3.7 Figures

Figure 3.1 Schematic of the electrodeposition set-up. Three electrode cell is immersed in a silicone oil bath, which the temperature was controlled by a thermocouple connected to a hot plate.

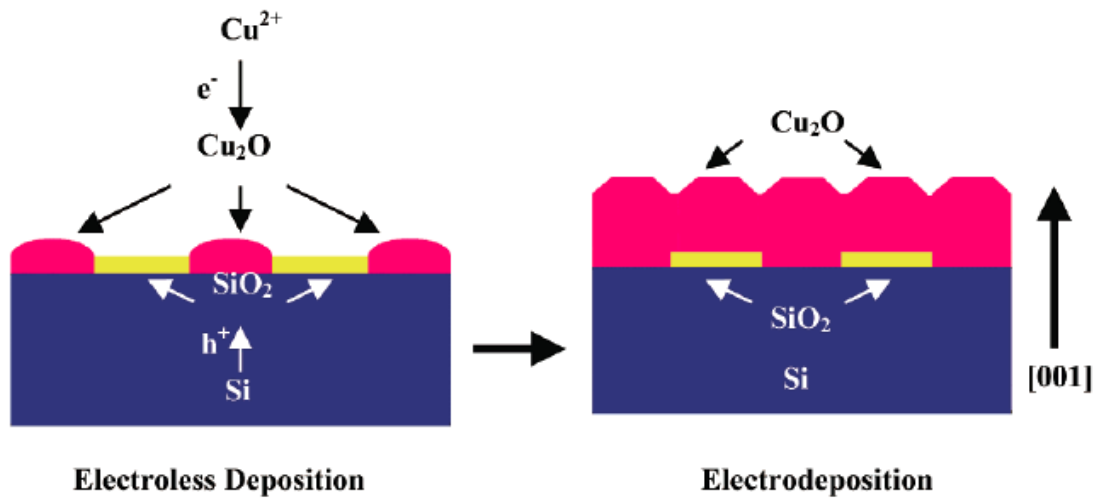**Electroless Deposition**　　　　　**Electrodeposition**

Figure 3.2 Proposed deposition schematic by Switzer [47]. Prior to the deposition, silicon is etched by HF to remove the native oxide layer and expose the silicon, such as that copper (I) oxide seeds can be deposited onto the silicon as seeds. Only after this treatment, does the electrodeposition proceed.
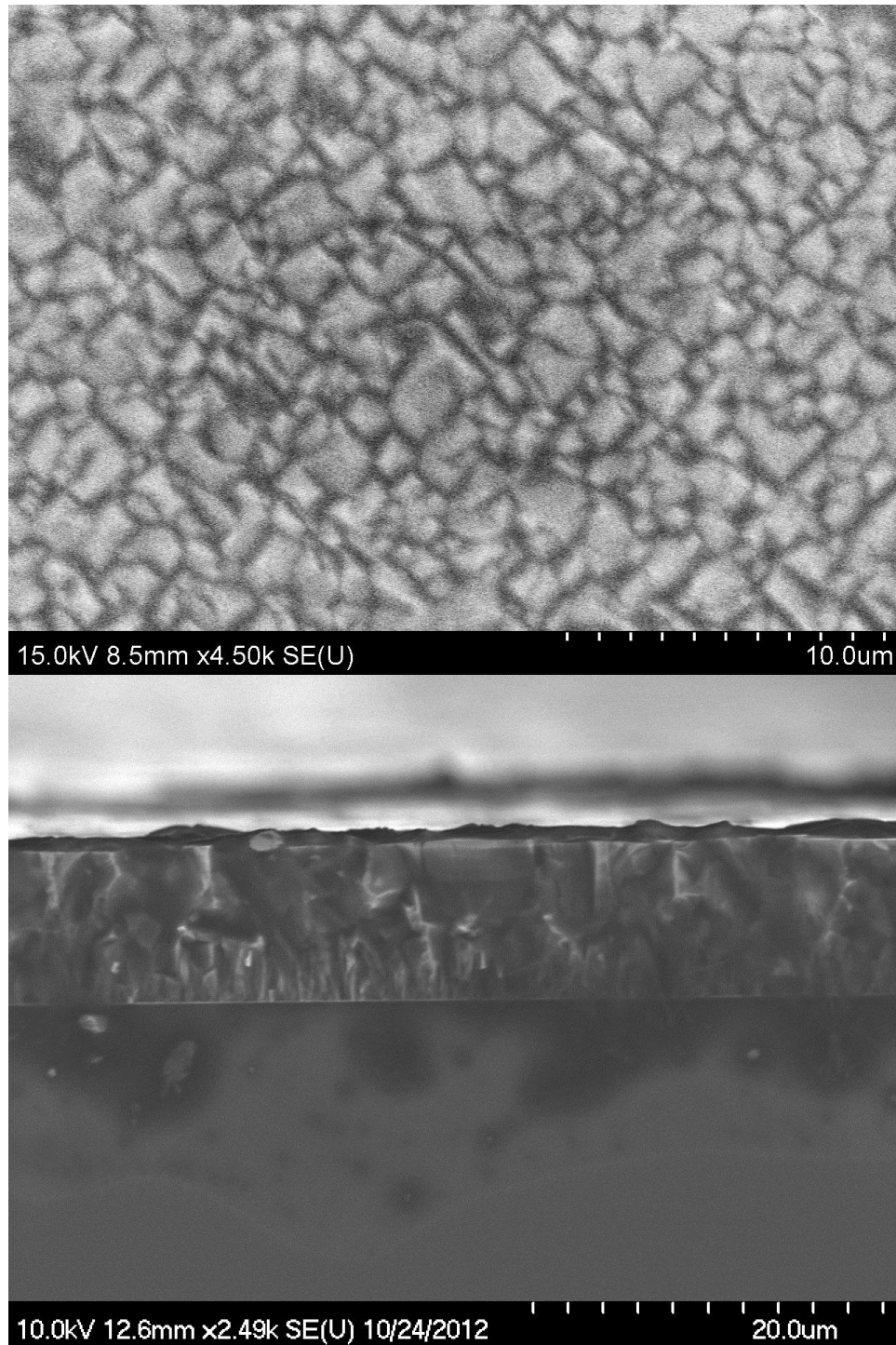
Figure 3.3 SEM Images of Cu₂O deposited onto silicon film. Top view shows an aligned squares and pyramids on the top image. Cross-sectional view is shown on the bottom image.
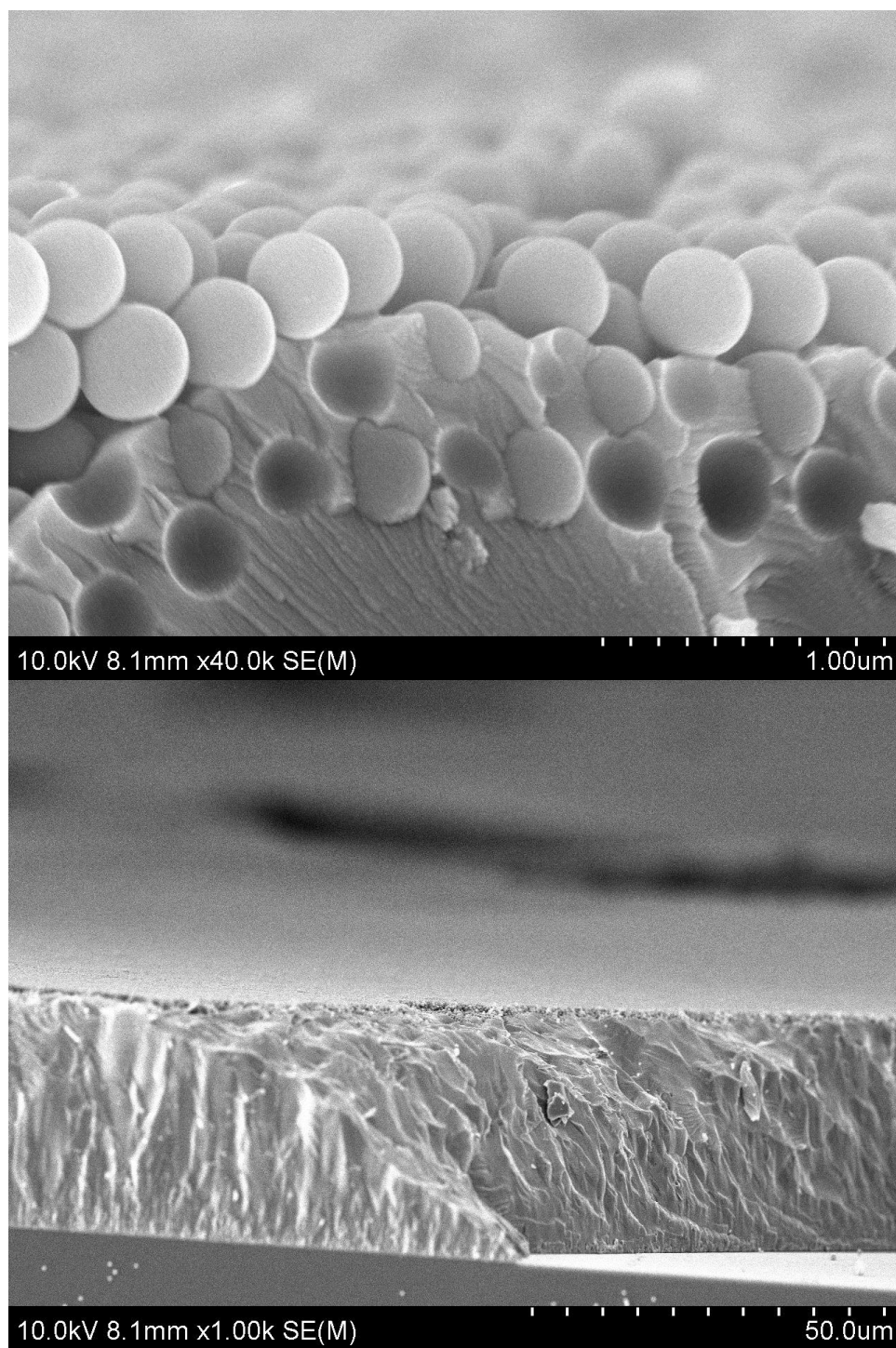
Figure 3.4 Cross-sectional SEM image of successful deposition of Cu_2O inside the opal structure (TOP).   The opal structures were grown onto cuprous oxide film deposited onto silicon before infilling the structure with electrodeposition. Bottom image is the SEM cross-sectional image of the Cu_2O film on which the opal was grown.
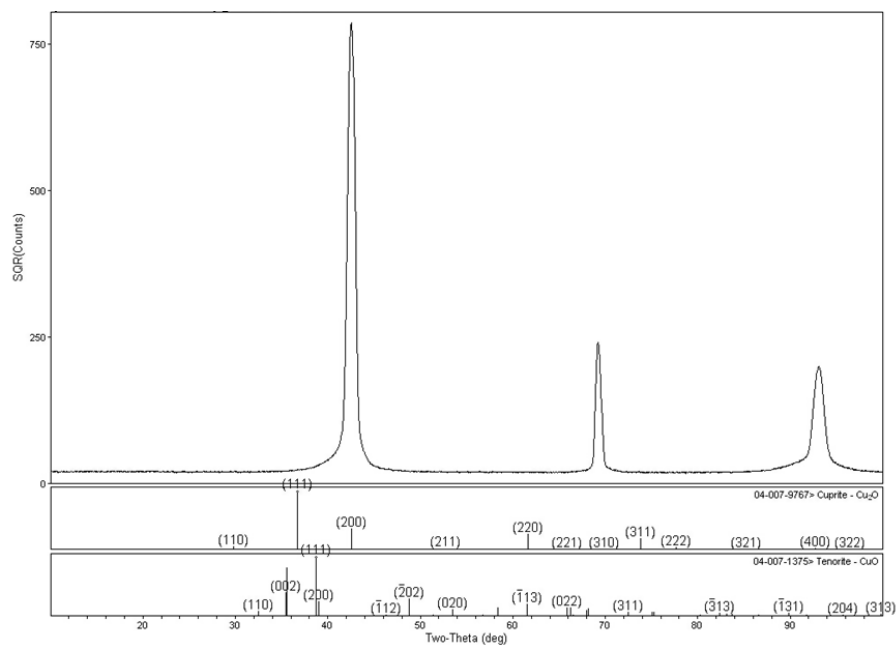
Figure 3.5 Representative omega-2theta XRD scan of the cuprous oxide film is shown. The peak at 69° corresponds to silicon (004) peak. The top profile is that of the cuprite, Cu_2O and the bottom is the XRD profile of tenorite, CuO. None of the peaks of tenorite match well with that measured. Meanwhile, the two other peaks correspond to that of (200) and (400) orientation of Cu_2O.
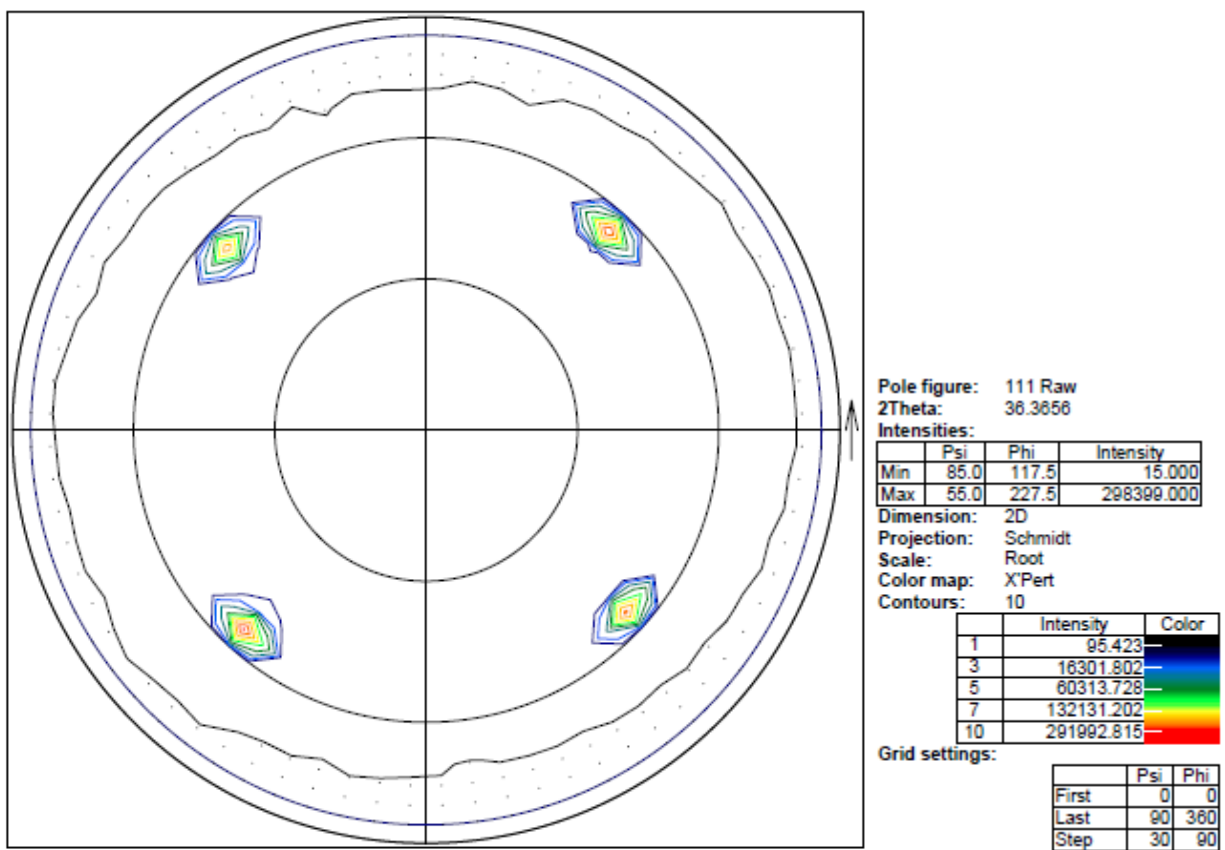
Figure 3.6 Representative pole figure taken from (111) orientation of the Cu_2O ($2\theta = 36.3656°$) on the as grown Cu_2O film from Figure 3.5.
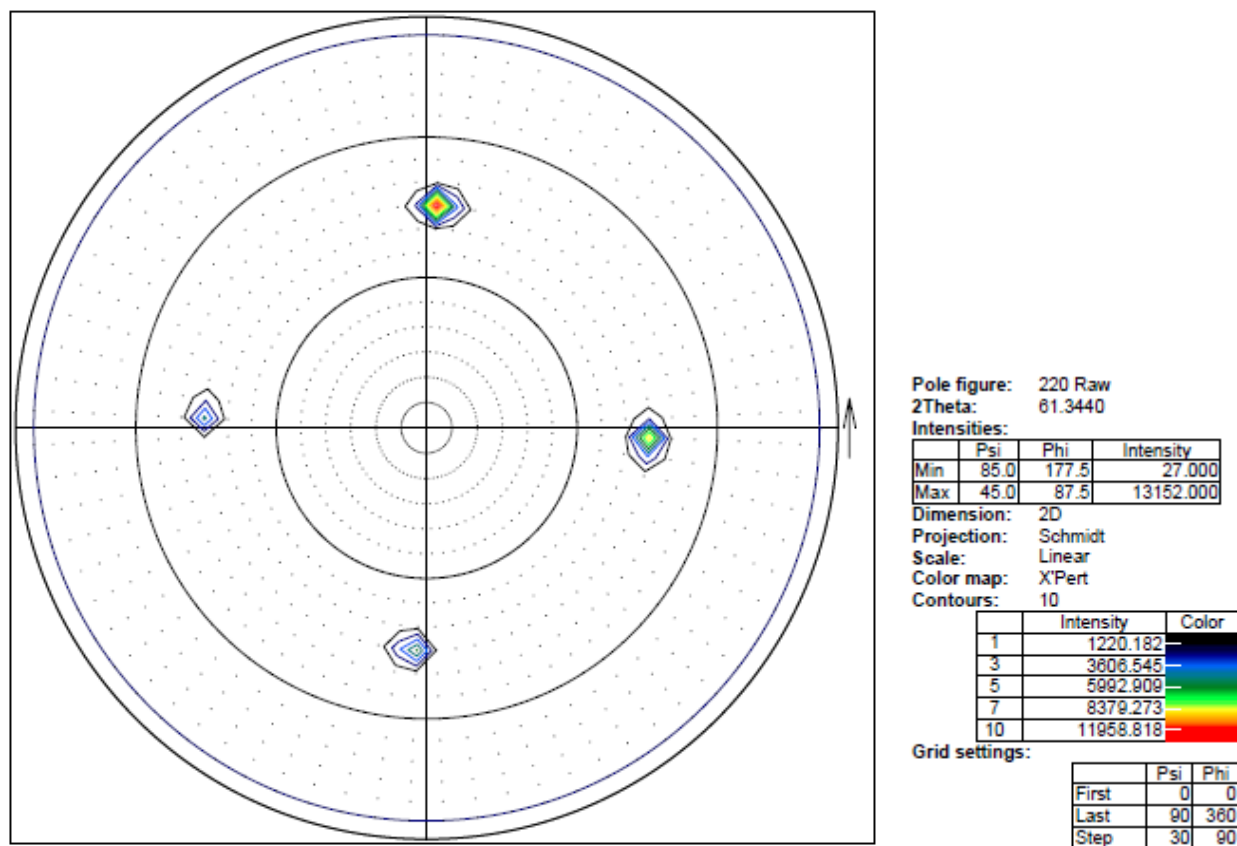
Figure 3.7 Representative pole figure taken from (220) orientation of the Cu_2O ($2\theta = 61.344°$) on the as grown Cu_2O film. Pole figure of this was taken from a different sample from that of Figures 3.5 and 3.6, but a sample showing similar XRD profile with much lower intensity.
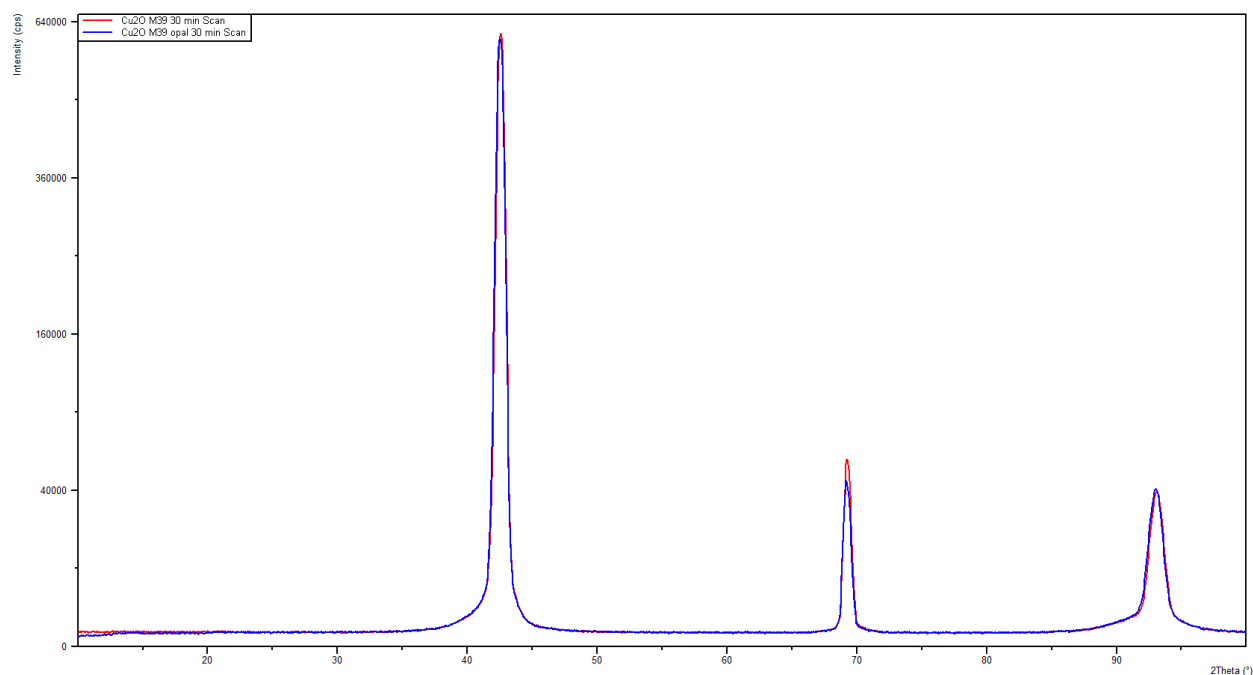
Figure 3.8 XRD profile comparison between that of the as grown film (red, Figure 3.5) and of the Cu_2O inverse opal grown from the same film (blue). Due to the thickness of the sample, no change was seen. The only change that occurred is the slight decrease in the intensity of the silicon peak after the growth of the opal. The ratio of Cu_2O (002) to Si (004) did increase from 10.69 in red to 13.45 in blue.

Pole figure: 111 Raw
2Theta: 36.3656
Intensities:

|	Psi	Phi	Intensity
Min	85.0	197.5	2.000
Max	55.0	47.5	293113.000

Dimension: 2D
Projection: Schmidt
Scale: Root
Color map: X'Pert
Contours: 10

	Intensity	Color
1	53.051	
3	15543.017	
5	58592.878	
7	129202.634	
10	286792.073	

Grid settings:

	Psi	Phi
First	0	0
Last	90	360
Step	30	90
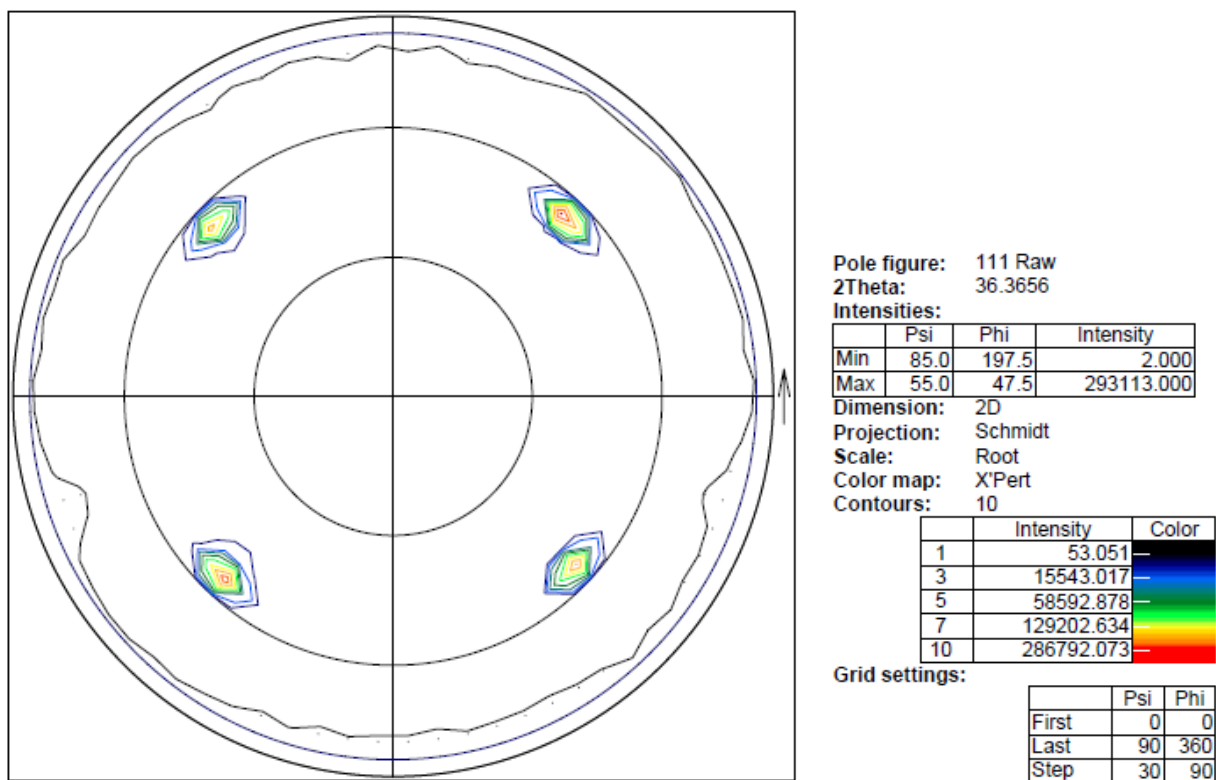
Figure 3.9 A pole figure from the (111) orientation after the opal filling. Same sample as that of the blue graph in Figure 3.8.
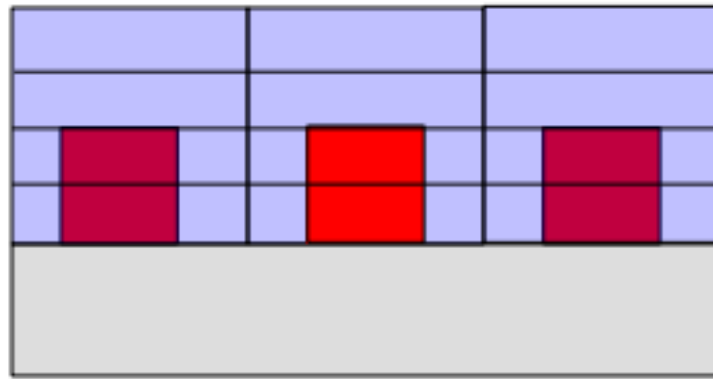
Ideal epitaxy
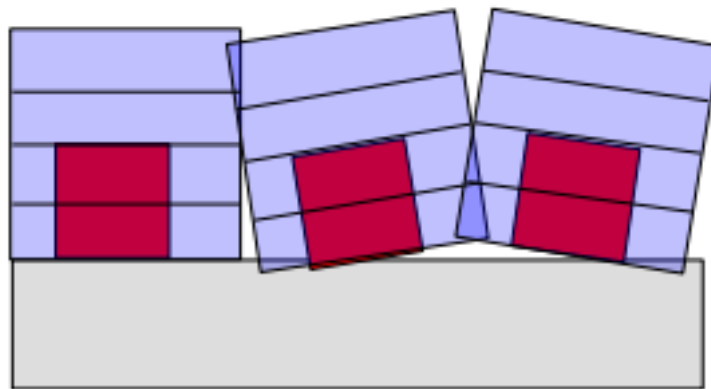
Textured Epitaxy

Figure 3.10. Schematic showing an ideal epitaxy case and a textured epitaxy case, the latter of which has a "mosaic spread."
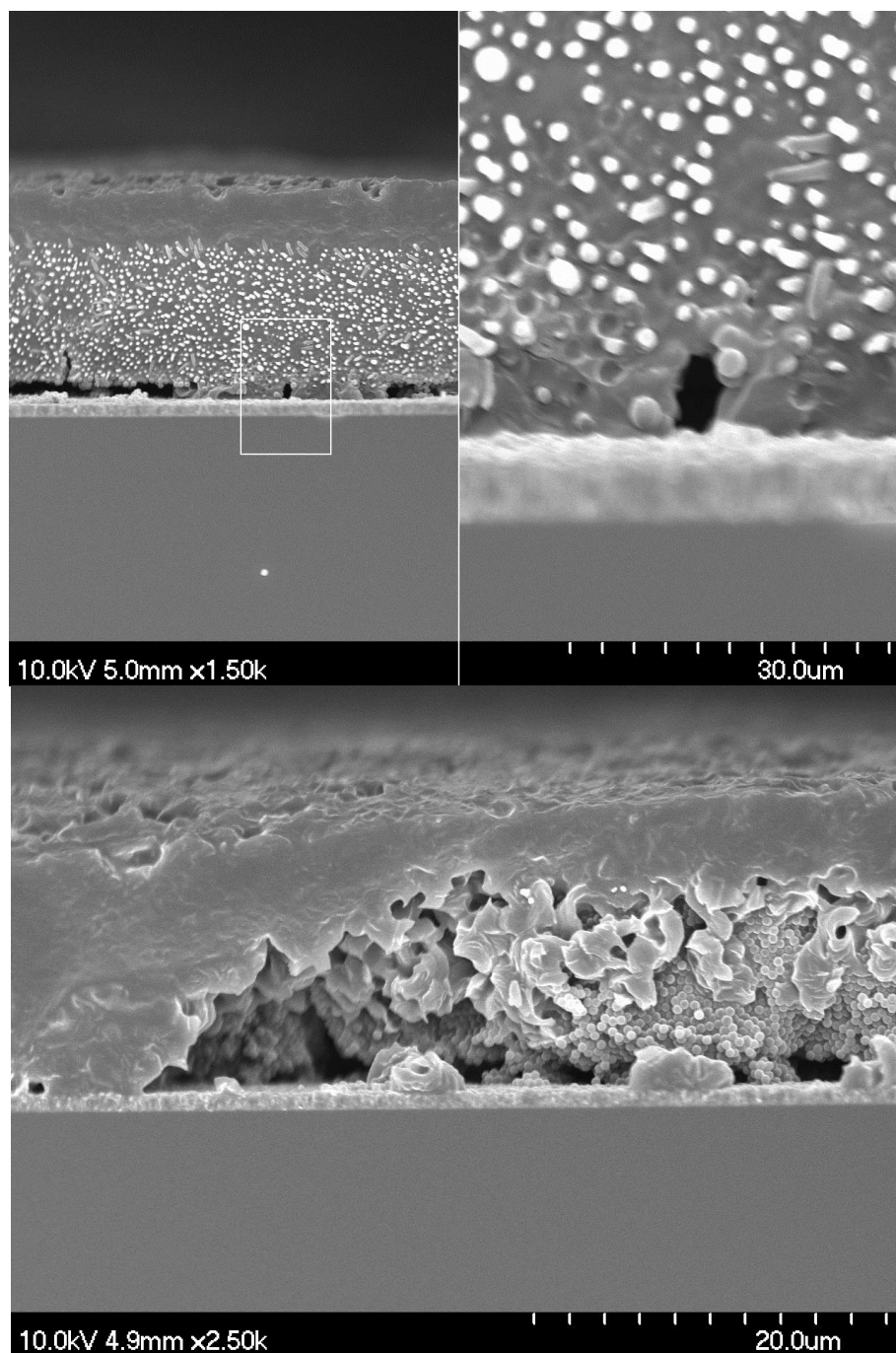
Figure 3.11 Cross-sectional SEM images of Cu_2O deposition attempt into 500 nm polystyrene opal structure grown on top of Cu_2O film. The scale bar for the top image corresponds to the image on the left and the right image is just zoomed in to the rectangular area specified on the right.
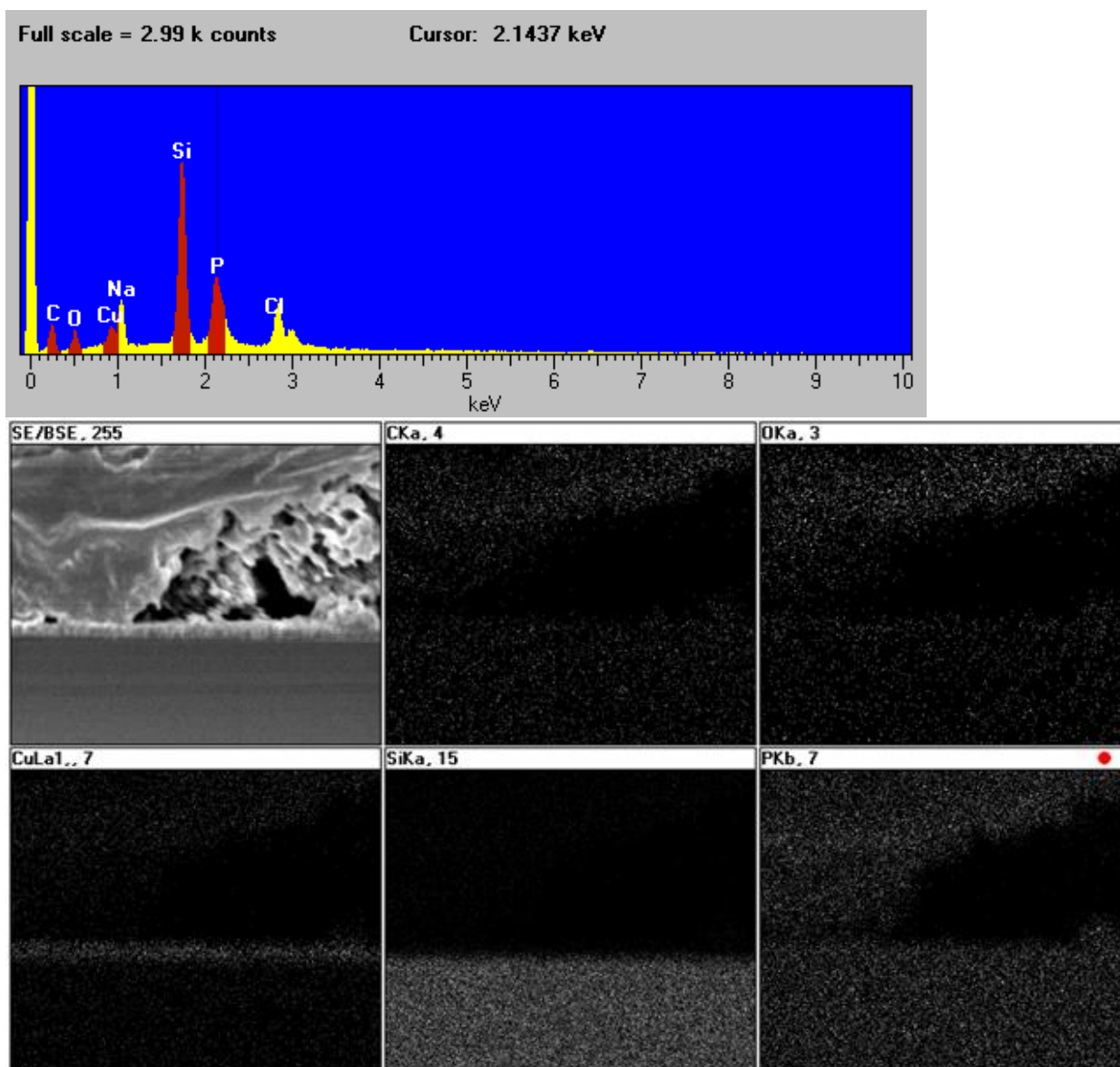
Figure 3.12 EDS spectra and mapping obtained by scanning the area shown on Figure 3.11 bottom SEM image. Top shows the spectra which show impurities of phosphorus and sodium. Sodium likely came from the added sodium hydroxide from the electrolyte and the phosphorus is the dopant used on the silicon. It can be seen that the material on top for the copper oxide film just above the silicon wafer is not copper material. This unknown material consists of carbon, oxygen, and phosphorus as shown by the mapping.

CHAPTER 4

CONCLUSIONS

As engineering devices approach nanometer scale, detailed knowledge of thermal transport is needed. Sub 100 nanometer, three-dimensional inverse opal structures provide an ideal structure to conduct multi-dimensional nano-scale thermal transport studies, and this investigation laid the founding work into creating such structures.

Using synthesized sub 100 nanometer silica nanoparticles, sub 100 nanometer porous structures can be fabricated via colloidal assembly. For the inverse silicon nanostructure, silicon was successfully deposited into this sub 100 nanometer periodic silica opal structure using a static chemical vapor deposition method.

Meanwhile, beginning works into creating eptiaxial Cu_2O inverse opal structure was demonstrated. Cu_2O successfully deposited electrochemically into a silica opal structure of much larger size (400 nm). X-ray analysis strongly suggests epitaxial nature of the cuprous oxide, but further materials characterization is required. Using parallel structures that are sub-100 nanometers in size, Cu2O could perhaps be deposited in an epitaxial manner.

Despite the successful deposition, optimization of the material is needed. Several attempts to study the thermal property of nanostructured silicon did not succeed. Altering the procedure slightly to improve the structural property for thermal measurement is needed. Furthermore, cuprous oxide presents issues with the silica etching, which can act as umklapp phonon scattering sites that can affect the nano-thermal study. Additional work is required for the thermal study, but this research lays out the groundwork for materials processing to fabricate nanostructures suitable for multi-dimensional thermal study on the nanoscale.

REFERENCES

1. Cahill, D. G.; Ford, W. K.; Goodson, K. E.; Mahan, G. D.; Majumdar, A.; Maris, H. J.; Merlin, R.; Phillpot, S. R., Nanoscale thermal transport. *Journal of Applied Physics,* **2003**, 93, 793-818.

2. Chang, C.W.; Okawa, D.; Garcia, H.; Majumdar, A.; Zettl, A., Breakdown of Fourier's Law in Nanotube Thermal Conductors. *Physical Review Letters*, **2008**, 101, 075903.

3. Minnich, A. J.; Dresselhaus, M. S.; Ren, Z. F.; Chen, G., Bulk Nanostructured Thermoelectric Materials: Current Research and Future Prospects. *Energy & Environmental Science,* **2009**, 2, 466-479.

4. Cahill, D. G.; Watson, S.K.; Pohl, R. O., Lower limit to the thermal conductivity of disordered crystals., *Physical Review B*, **1992**, 46 (10), 6131-6140.

5. Costescu, R. M.; Cahill, D. G.; Fabreguette, F. H.; Sechrist, Z. A.; George, S. M., Ultra-Low Thermal Conductivity in W/Al_2O_3 Nanolaminates, *Science*, **2004**, 303 (5660), $989 - 990$.

6. Chiritescu, C.; Cahill, D.G.; Nuyen, N.; Johnson, D.; Bodapati, A.; Keblinski, P.; Zschack, P., Ultralow Thermal Conductivity in Disordered, Layered WSe_2 Crystals. *Science*, **2007**, 315, 351-353.

7. Vineis, C. J.; Shakouri, A.; Majumdar, A.; Kanatzidis, M. G., Nanostructured Thermoelectrics: Big Efficiency Gains from Small Features. *Advanced Materials,* **2010**, 22 (36), $3970 - 3980$.

8. Hochbaum, A. I.; Chen, R.; Delgado, R. D.; Liang, W.; Garnett, E. C.; Najarian, M.; Majumdar, A.; Yang, P., Enhanced thermoelectric performance of rough silicon nanowires., *Nature*, **2008**, 451, $163 - 167$.

9. Boukai, A. I.; Bunimovich, Y.; Tahir-Kheli, J.; Yu, J.; Goddard III, W. A., Heath, J. R., Silicon nanowires as efficient thermoelectric materials, *Nature*, **2007**, 451, 168-172.

10. Biswas, K.; He, J.; Blum, I. D.; Wu, C.; Hogan, T.; Seidman, D. N.; Dravid, V. P.; Kanatzidis, M.G., High-performance bulk thermoelectrics with all-scale hierarchical architectures., *Nature*, **2012**, 489, $414 - 418$.

11. Chen, G.; Dresselhaus, M. S.; Dresselhaus, G.; Fleurial, J. P.; Caillat, T., Recent Developments in Thermoelectric Materials. *International Materials Reviews*, **2003**, 48 (1) $45 - 66$.

12. Kushwaha, M. S.; Halevi, P.; Dobrzynski, L.; Djafari-Rouhani, B.; Acoustic Band Structure of Periodic Elastic Composites., *Physical Review Letters*, **1993**, 71 (13), $2022 - 2025$.

13. Vasseur, J. O.; Deymier, P. A.; Khelif, A.; Lambin, P.; Djafari-Rouhani, B.; Akjouj, A.; Dobrzynski, L.; Fettouhi, N.; Zemmouri, J., Phononic crystal with low filling fraction and absolute acoustic band gap in the audible frequency range: A theoretical and experimental study., *Physical Review E*, **2002**, 65, 056608.

14. Lee, J.H.; Galli, G. A.; Grossman, J. C., Nanoporous Si as an Efficient Thermoelectric Material, *Nano Letters,* **2008**, 8 (11), 3750 − 3754.

15. Yang, L.; Yang, N.; Li, B., Reduction of Thermal Conductivity by Nanoscale 3D Phononic Crystal., *Scientific Reports*, **2013**, 3, 1 − 5.

16. Tang, J.; Wang, H.; Lee, D. H.; Fardy, M.; Huo, Z.; Russell, T. P.; Yang, P., Holey silicon as an Efficient Thermoelectric Material., *Nano Letters*, **2010**, 10, 4279 − 4283.

17. Yu, J.; Mitrovic, S.; Tham, D.; Varghese, J.; Heath, J. R., Reduction of thermal conductivity in phononic nanomesh structures, *Nature Nanotechnology*, **2010**, 5, 718 − 721.

18. Luckyanova, M. N.; Garg, J.; Esfarjani, K.; Jandl, A.; Bulsara, M. T.; Schmidt, A. J.; Minnich, A. J.; Chen, S.; Dresselhaus, M. S.; Ren, Z.; Fitzgerald, E. A.; Chen, G., Coherent Phonon Heat Conduction in Supperlattices, *Science*, **2012**, 338, 936 − 938.

19. J. Ma, B.R. Parajuli, M.G. Ghossouh, A. Mihi, J. Sadhu, P.V. Braun and S. Sinha: Coherent Phonon-Grain Boundary Scattering in Silicon Inverse Opals, *Nano Letters*, **2013**, 13, 618-624.

20. Leong, M.; Doris, B.; Kedzierski, J.; Rim, K.; Yang, M., Silicon Device Scaling to the Sub-10-nm Regime., *Science*, **2004**, 306, 2057 − 2060.

21. Davis, J. A.; Venkatesan, R.; Kaloyeros, A.; Beylansky, M.; Souri, S. J.; Banerjee, K.; Saraswat, K. C.; Rahman, A.; Reif, R.; Meindl, J. D., Interconnect Limits on Gigascale Integration (GSI) in the 21st Century. *Proceedings of the IEEE*, **2001**,89 (3), 305-324.

22. King, W. P.; Kenny, T. W.; Goodson, K. E.; Cross, G.; Despont, M. *et al.* Atomic force microscope cantilevers for combined thermomechanical data writing and reading. *Applied Physics Letters*, **2001**, 78, 1300 - 1302.

23. M. G. Holland, Analysis of Lattice Thermal Conductivity. *Physical Review*, **1963**, 132, 2461 -2471.

24. Yu, X.; Braun, P. V.; Assembly and Functionalization of 3D Photonic Crystals, *Proceedings of ISAF 2008*, **2008**, 2, 1-2

25. Rinee, S. A.; Garcia-Santamaria, F.; Braun, P. V., Embedded cavities and waveguides in three-dimensional silicon photonic crystals., *Nature Photonics*, **2008**, 2, 52 − 56.

26. Dai, Z.; Yu, X.; Zhang, H.; Kim, T.; Braun, P. V.; King, W. P., Photonic Crystal Nickel and Aluminum Oxide Micromechanical Devices Having 3D Inverse Opal Microstructure, *MEMS 2011*, **2011**, 308 -311, Cancun, Mexico.

27. Stöber, W; Fink, A; Bohn, E., Controlled Growth of Monodisperse Silica Spheres in the Micron Size Range, *Journal of Colloid and Interface Science*, 1968, 26 (1), 62-69.

28. Zhao, X.; Bagwe, R.; Tan, W., Development of Organic-Dye-Doped Silica Nanoparticles in a Reverse Microemulsion. *Advanced Materials*, **2004**, 16 (2), 173-176.

29. Bogush, G.; Tracy, M.; Zukoski, C., Preparation of Monodisperse Silica Particles: Control of Size and Mass Fraction. *Journal of Non-Crystalline Solids*, **1988**, 104, 95-106.

30. Chabanov, A. A.; Jun, Y.; Norris, D., Avoiding Cracks in Self-assembled Photonic Band-gap Crystals, *Applied Physics Letters,* 2004, 84 (18), 3573−3575

31. Jiang, P.; Bertone, J.F.; Hwang, K.S.; Colving, V. L., Single Crystal Colloidal Multilayers of Controlled Thickness, *Chemistry of Materials*., **1999**, 11 (8), 2132-2140.

32. David G. Cahill, Thermal conductivity measurement from 30 to 750K: the 3ω method, *Review of Scientific Instruments*, **1990**, 61 (2), 802 – 808.

33. David G. Cahill, Analysis of heat flow in layer structures for time-domain thermoreflectance., *Review of Scientific Instruments*, **2004**, 75 (12), 5119 – 5122.

34. Takahagi, t.; Nagai, I.; Ishitani, A.; Kuroda, H.; Nagasawa, Y., The formation of hydrogen passivated silicon single-crystal surfaces using ultraviolet cleaning and HF etching. *Journal of Applied Physics*, **1988**, 64, 3516 – 3521.

35. Jun Ma and Sanjiv Sinha, Thermoelectric properties of highly doped n-type polysilicon inverse opals, *Journal of Applied Physics*, **2012**, 112, 073719.

36. Chen, Y.; Bagnall, D. M.; Koh, H.; Park, K.; Hiraga, K., et al., Plasma assisted molecular beam epitaxy of ZnO on c-plane sapphire: Growth and Characterization. *Journal of Applied Physics*, **1998**, 84, 3912 – 3918.

37. Goldberger, J.; He, R.; Zhang, Y.; Lee, S.; Yan, H.; Choi, H.; Yang, P., Single-crystal gallium nitride nanotubes., *Nature*, **2003**,, 422, 599 – 602.

38. Chambers, S. A., Thevuthasan, S.; Farrow, R. F. C.; Marks, R. F.; Thiele, J. U. et al., Epitaxial growth and properties of ferromagnetic co-deoped TiO_2 anatase., *Applied Physics Letters*, **2001**, 79, 3467 – 3469.

39. Nelson, E. C.; Dias, N.; Bassett, K.; Dunham, S.; Verma, V.; Miyake, M.; Wiltzius, P.; Rogers, J.; Coleman, J.; Li, X.; Braun, P. V., Epitaxial growth of three-dimensionally architecture optoelectronic devices., *Nature Materials*, **2011**, 10, 676 - 681.

40. Gregory, B. W. and Stickney, J. L., Electrochemical atomic layer epitaxy (ECALE), *Journal of Electroanalytical Chemistry and Interfacial Electrochemistry*, **1991**, 300, 543 – 561.

41. Bohannan, E. W.; Shumsky, M. G.; Switzer, J. A., Epitaxial Electrodeposition of Copper(I) Oxide on Single-Crystal Gold (100), *Chemistry of Materials*, **1999**, 11, 2289 – 2291.

42. Barton, J. K.; Vertegel, A. A.; Bohannan, E. W.; Switzer, J. A., Epitaxial Electrodeposition of Copper(I) oxide on Single-Crystal Copper., *Chemistry of Materials*, **2001**, 13, 952 – 959.

43. Oba, F.; Ernst, F.; Yu, Y.; Liu, R.; Kothari, H. M.; Switzer, J., Epitaxial Growth of Cuprous Oxide Electrodeposited onto Semiconductor and Metal Substrates., *Journal of American Ceramics Society*, **2005**, 88 (2), 253 – 270.

44. Braun, P. V.; Wiltzius, P., Electrochemical Fabrication of 3D Microperiodic Porous Materials. *Advanced Materials*, **2001**, 13 (7), 482 – 485.

45. A. E. Rakhsani, Preparation, Characteristics, and Photovoltaic Properties of Cuprous Oxide – A Review*., Solid-State Electronics*, **1986**, 29 (1), 7- 17.

46. Chen, X.; Parker, D.; Du, M.; Singh, D.J., Potential thermoelectric performance of hole-doped Cu2O, *New Journal of Physics*, **2013**, 15, 043029.

47. Switzer, J. A.; Liu, R.; Bohannan, E. W.; Ernst, F., Epitaxial Electrodeposition of a Crystalline Metal Oxide onto Single-Crystalline Silicon., *Journal of Physical Chemistry B*, **2002**, 106, 12369 -12372.

48. Thanu, D. P. R.; Venkataraman, N.; Raghavan, S.; Mahdavi, O., Dilute HF Solutions for Copper Cleaning during BEOL Processes: Effect of Aeration on Selectivity and Copper Corrosion., *ECS Transacations*, **2009**, 25 (5), 109 – 116.